Effects of dynamic changes of desiccation cracks on preferential flow: Experimental investigation and numerical modeling

Yi Luo[1,2], Jiaming Zhang*[1], Zhi Zhou[3], Juan P. Aguilar-Lopez[4], Roberto Greco[5], Thom Bogaard[2]

[1] Faculty of Engineering, China University of Geosciences (Wuhan), Wuhan, 430074, China

[2] Water Resources Section, Faculty of Civil Engineering and Geosciences, Delft University of Technology, Stevinweg 1, P.O. Box 5048, 2600 GA Delft, the Netherlands

[3.] Department of Engineering Management, Hubei University of Economics, Wuhan, 430205, China

[4.] Department of Hydraulic Engineering, Faculty of Civil Engineering and Geosciences, Delft University of Technology, Delft, 2600 GA, the Netherlands

[5.] Dipartimento di Ingegneria, Università degli Studi della Campania "Luigi Vanvitelli", via Roma 29, 81031, Aversa, Italy

Correspondence to: Jiaming Zhang (zjm@cug.edu.cn)

Abstract: Preferential flow induced by desiccation cracks (PF-DC) has been proven to be an important hydrological effect that could cause various geotechnical engineering and ecological environment problems. Investigation on the PF-DC remains a great challenge due to the soil shrinking-swelling behavior. This work presents an experimental and numerical study of the PF-DC considering the dynamic changes of DC. A soil column test was conducted under wetting-drying cycles to investigate the dynamic changes of DC and their hydrological response. The ratio between the crack area and soil matrix area (crack ratio), crack aperture and depth were measured. The soil water content, matrix suction and water drainage were monitored. A new dynamic dual-permeability preferential flow model (DPMDy) was developed, which includes physically-consistent functions in describing the variation of both porosity and hydraulic conductivity in crack and matrix domains. Its performance was compared to the single-domain model (SDM) and rigid dual-permeability model (DPM) with fixed crack ratio and hydraulic conductivity. The experimental results showed that the maximum crack ratio and aperture decreased when the evaporation intensity was excessively raised. The self-closure phenomenon of cracks and increased surficial water content were observed during low evaporation periods. The simulation results showed that the matrix evaporation modeled by the DPMDy is lower than that of the SDM and DPM, but its crack evaporation is the highest. Compared to the DPM, the DPMDy simulated a faster pressure head building-up process in the crack domain and higher water exchange rates from the crack to the matrix domain during rainfall. Using a fixed crack ratio in the DPM, whether it is the maximum or the average value from the experiment data, will overestimate the infiltration fluxes of PF-DC but underestimate its contribution to the matrix domain. In conclusion, the DPMDy better described the underlying physics involving crack evolution and hydrological response with respect to the SDM and DPM. Further improvement of the DPMDy should focus on the hysteresis effect of the soil water retention curve and soil deformation during wetting-drying cycles.

Keywords: Desiccation cracks; preferential flow; dynamic changes; dual-permeability model; wetting-drying cycles

1. Introduction

Desiccation cracks are prevalent in clay-dominated soils due to water loss, which often lead water to bypass the surface soil matrix and rapidly infiltrate into subsoil as preferential flow (Davidson, 1984; Weiler, 2005). Positively, the preferential flow induced by desiccation cracks (PF-DC) can promote the migration of farmland organic matter (Vervoort et al., 2003) and reduce surface runoff (Pei et al., 2020; Zhang et al., 2021a). Negatively, it also has proven to be an important hydrological

mechanism that could lead to geotechnical engineering and ecological environment problems, such as dike and slope instability (Jamalinia et al., 2020; Zhang et al., 2021b), shallow landslides (Bogaard and Greco, 2015; Caris and Van Asch, 1991; Luo et al., 2021), groundwater pollution (Chaduvula et al., 2022; Chen et al., 2002; Mooney and Morris, 2008; Schlögl et al., 2022) and reduction of irrigation efficiency (Greve et al., 2010; Smith et al., 2005; Wang et al., 2018; Wang et al., 2022). Under the current background of frequent extreme flood-drought climate events, its negative effects will be more prominent (Tichavsky et al., 2019). Investigation on the PF-DC are of great significance in guiding scientific research and practical design in the above disciplines.

A unique characteristic of the desiccation cracks is their dynamic features, often causing instantaneous variation of crack proportion, depth and connectivity with moisture content. Previous efforts have attempted to reveal the effects of crack dynamics on the PF-DC through experimental studies, but most of them focused on short-term wetting process and obtained only qualitative results and debates remained. For instance, Favre et al. (1997)and Liu et al. (2003) stated that crack closure due to wetting can cause a significant reduction or even disappearances in the preferential flow. However, other studies found that the PF-DC also leads water to rapidly infiltrate into deep soil even when desiccation cracks are nearly closed (Baram et al., 2012a; Greve et al., 2010; Luo et al., 2021; Tuong et al., 1996; Sander and Gerke, 2007). Cheng et al. (2021) conducted a series of constant-head permeability tests with the hydraulic head gradient of 15 kPa. They stated that 4% of surface crack ratio could be a critical value for determining whether desiccation cracks cause a significant increase in the infiltration rate or not. However, this value may vary with different soils, rainfall patterns and sample scales, and thus lacks general applicability. Indeed, PF-DC has long-term and complex spatiotemporal variability due to crack dynamics during wetting-drying cycles. Therefore, short-term and small-scale infiltration tests (i.e. laboratory permeability tests) are not enough to reveal the complex hydrological process induced by PF-DC. Meanwhile, it is also difficult to quantitatively study PF-DC only through experiments. An improve understanding of the PF-DC combined with theoretical methods is also needed.

Regarding the theoretical methods, explicit crack models (EMs) (Hendrickx. and Flury, 2001; Khan et al., 2017; Xie et al., 2020)), dual-porosity (DPoM) (Van Genuchten, 1980; Van Genuchten and Wierenga, 1976) and dual-permeability (DPM) (Aguilar‑López et al., 2020; Gerke and Van Genuchten, 1993b, 1993a) models were developed to simulate preferential flow in cracked clay soils. EMs were constructed based on the single-domain (or single-permeability) framework, which require to define the details involving the geometry, spatial distribution and hydrological properties of each crack. Such requirement may be conceptually correct but makes them difficult for simulating network-distributed desiccation cracks due to considerable computational burden (Aguilar‑López et al., 2020). The DPoM and DPM concepts belong to the dual-domain framework that assumes the soil pore system can be represented as two overlapping interacting regions, one which represents the matrix domain with micropores and the other one represents the crack domain with meso-macro pores (Šimůnek et al., 2003). Those models represent the cracks in the soil as implicit form which need not to prescribe geometrical and spatial features of the desiccation cracks. The DPoM concept holds the simplifying stipulation that water only flows through the shrinkage cracks rather than the soil matrix, which is unrealistic in many cases. To remedy this shortcoming, classical DPM was developed, where, the water flow in soil matrix and crack domain was simulated using the Richards' equation (Aguilar‑López et al., 2020; Coppola et al., 2012; Gerke and Maximilian Köhne, 2004; Gerke and Van Genuchten, 1993a) or Green-Ampt model (Davidson, 1984; Stewart, 2019; Weiler, 2005) building on Darcy's law. However, some critics emerged that the Richards' equation building on the capillarity, not existing in large PF paths (e.g. tensile cracks and biological holes), is not suitable to simulate the PF (Larsbo and Jarvis, 2003; Nimmo, 2010; 2021). Consequently, some improved DPMs were developed, where, water flow in the crack domain was simulated by the Navier-Stokes equation (Germann and Karlen, 2016; Nimmo, 2010), kinematic wave equation (Greco, 2002; Larsbo and Jarvis, 2003) and Poiseuille model (Lepore et al., 2009). Although these improved DPM models better captured the characteristics of the water flow in the crack domain, the classical DPM concept has still been widely accepted and used in simulating preferential flow in soils due to its easily available

81 parameters, reasonably satisfactory prediction to the measurements and high computation efficiency (Jarvis et al., 2016). Most

82 importantly, a recent numerical study conducted by Aguilar‑López et al. (2020) proved that effective parameter selection in

83 the DPM models can achieve similar modeling results to the EMs.

84 Nevertheless, classical DPM models often adopt the assumption that crack volume and hydrological properties remain

85 constant in both time and space, which is unfeasible to capture the full dynamics of PF-DC. Some attempts have been made

86 to incorporate the dynamic nature of desiccation cracks into DPM including the SWAP family of models, i.e. LEACHM,

87 which simulates PF-DC using a shrinkage characteristic and water loss (Kroes et al., 2000), but neglects water exchange

88 process occurring at the interface between two domains. Such a process has widely been confirmed to be significant in cracked

89 soils (Greve et al., 2010; Krisnanto et al., 2016; Tuong et al., 1996). A later modification of SWAP incorporated the

90 aforementioned process, but at the cost of neglecting shrink-swell behavior of soil. The VIMAC model developed by Greco

91 (2002) solved previous problems but against the cost of inducing many parameters which are difficult to determine from

92 experiments or measurements. Coppola et al. (2012); (2015) took another step forward to allow crack volume and/or

93 hydrological properties to vary as a function of soil shrinkage. However, the relationship proposed in the model, an empirical

94 natural logarithm function involving the suction head and crack proportion, is not directly transferable to other types of soil. .

95 Stewart et al. (2016b) deduced a shrinking-swelling model, with relatively clear physical meaning and high consistency, and

96 recently incorporated it into a Green-Ampt based DPM (Stewart, 2018). While an analytical solution was obtained, the

97 intrinsic limitation of the Green-Ampt approach (i.e. hypothesis of the wetting front and request for a constant boundary

98 condition) hindered the further application of this model in complicated scenarios.

99 The objective of this research was to investigate the PF-DC from the experimental perspective in combination with an

100 effective modelling approach. Hence, a soil column test was conducted to investigate the dynamic changes of desiccation

101 cracks and hydrological response. The variation of crack geometry, including crack ratio, width and depth were measured.

102 The soil moisture content, matrix suction and water drainage were also monitored. Meanwhile, we developed a dynamic dual-

103 permeability preferential flow model by incorporating the shrinking-swelling model proposed by Stewart et al. (2016b). The

104 performance of the model was evaluated by comparing the simulated results with measured data.

2. Experimental study

105

106 2.1 Testing apparatus

107 To investigate the effects of dynamic changes of desiccation cracks on preferential flow, a soil column infiltration test was

108 conducted under wetting-drying cycles (abbreviated as WD cycles hereafter). The testing apparatus consisted of a rainfall-

109 evaporation system, environment monitoring device, a plexiglass column, HD camera, hydrological sensors and drainage

110 measurement device (Fig. 1).

111 The rainfall-evaporation system included a rainfall simulator and two warm lamps as well as a small fan. The rainfall simulator

112 was 0.5 m above the soil surface, which can produce rainfall with the intensity of 24-120 mm/h. The warm lamps and a small

113 fan were put near the soil surface to accelerate water evaporation. The environment monitoring device consisted of a thermo-

114 hygrometer that connected a probe above the soil surface to detect the environmental temperature and humidity, and a water

115 container to measure the potential evaporation.

116 The plexiglass column was composed of a column (with a height of 60 cm and a diameter of 50 cm) placed on a catchment

117 hopper which was used to collect and drain out water from the soil column.

118 HD camera (TTQ-J2, constant focal length: 35 mm) was fixed on the slope above the soil surface to take photos at regular

119 intervals during the drying periods.

120 Hydrological sensors, including 5 soil moisture content/temperature sensors (Acclima, TDR-310s, with a measurement

121 moisture content range of 0-100%, an accuracy of ±2%; temperature range of -40 ℃ - +60 ℃, an accuracy of ±0.2 ℃) and 5

122 water potential sensors (Campbell, WP-257, with a measurement range of -200 kPa - 0 kPa, an accuracy of ± 0.5 kPa), were

123 used to monitor the hydrological response during WD cycles. Five TDR-310s and five WP-257s were inserted into the soil

124 column from the two opposite sides of the plexiglass column, respectively, with the same height spacing of 10 cm from top

125 to bottom.

126 Drainage measurement device, including two electronic balances, were used to record the cumulative water drainage from

127 the soil column.
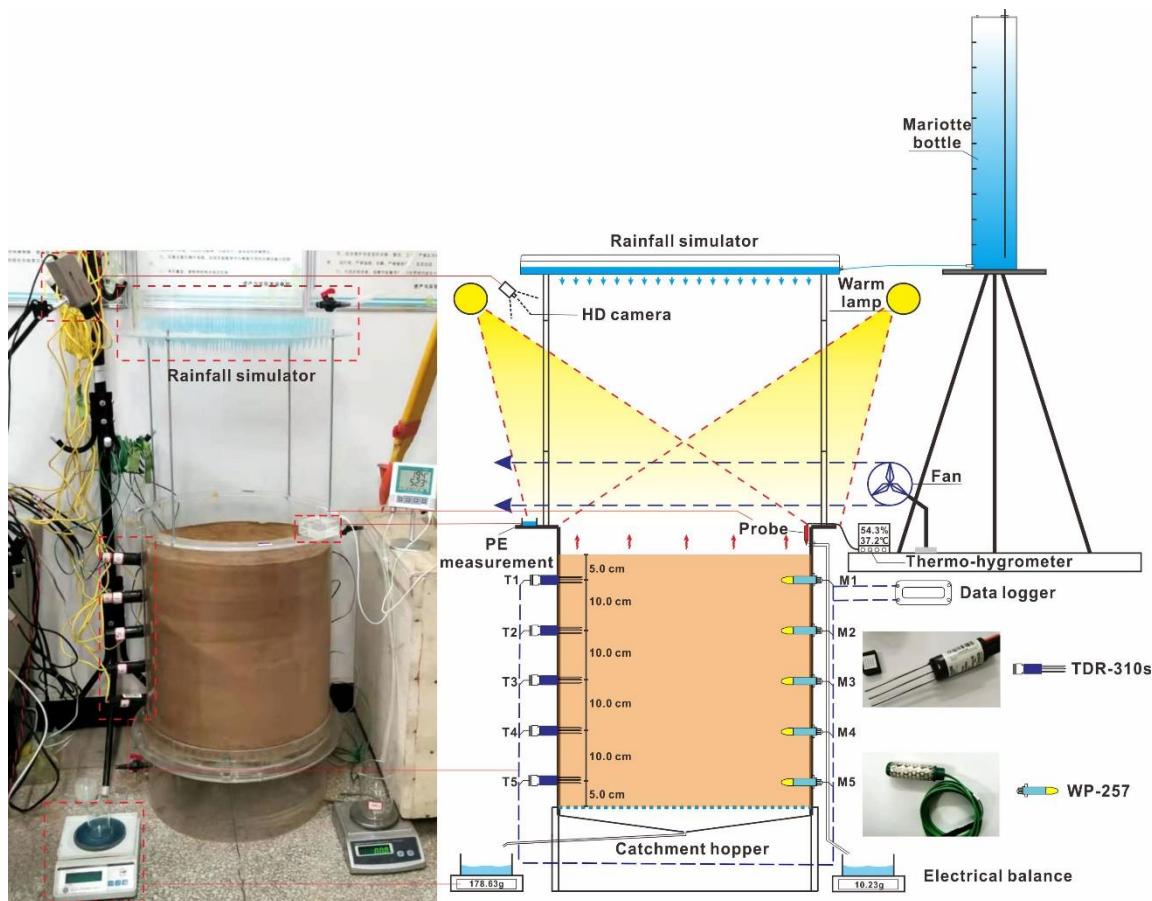
128

129 **Fig. 1** Schematic design and photos of the soil column test

130 2.2 Materials

131 The soil used in the test was taken from Zongyang county Anhui, China. Table 1 shows the basic physical parameters and

132 main mineral composition of the soil samples. The soil found in this study is classified as weak expansive soil. The saturated

133 hydraulic conductivity was measured on reconstituted soil cores with a dry density of 1.55g/cm³ (the same as the soil column).

134 In addition, the shrinkage curve of the saturated soil core was also obtained using a similar method proposed in Wen et al.

135 (2021). The difference is that we measured the vertical deformation in regular time intervals instead of continuous monitoring.

136 Fig. 2 shows the variation of soil porosity with the volumetric water content.

137 **Table 1** Basic physical parameters of the soil sample

Gs (-)	ω_{opt}	$\rho_{d,max}$	L_l (%)	P_l (%)	δ_{ef} (%)	C_{Illite}	$C_{Kaolinite}$	C_{Quartz}	C_{Albite}	K_s
2.73	0.17	1.7	38.7	18.9	42.7	43-57	4-12	34-47	0-11	8.3×10^{-7}-1.3×10^{-6}
Gs - specific gravity (-);										
ω_{opt} - optimal moisture content (g/g) which refers to the water content corresponding to the maximum dry density;										
$\rho_{d,max}$ – the maximum dry density (g/cm³);										
L_l - liquid limit (%); P_l - Plastic limit (%);										
δ_{ef} - Free swelling ratio (%);										
C_{Illite}, $C_{kaolinite}$, C_{Quartz} and C_{Albite} – content of illite, kaolinite, quartz and albite, respectively (%);										
K_s – Saturated hydraulic conductivity (m/s)										
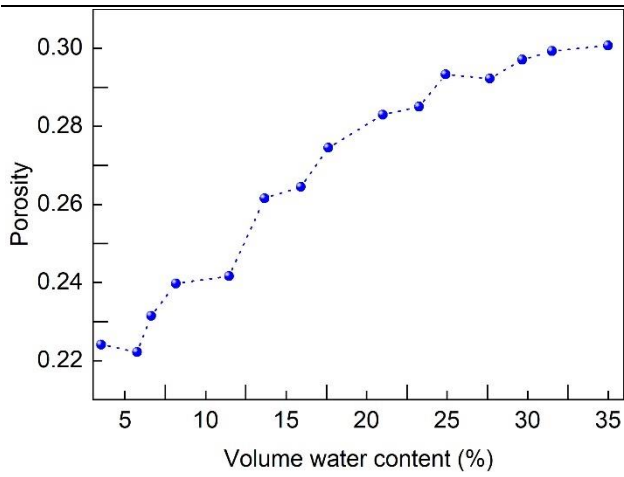
138

139 **Fig. 2** Shrinkage curve of the test soil

140 To ensure the homogeneity of the soil column, soil samples were compacted in 10 layers, and each layer was 5 cm thick. Prior

141 to filling soil into the plexiglass column, the soil samples with the total weight required for each layer were prepared according

142 to the designed density (dry density of 1.55g/cm³) and gravimetric water content (10%). Then, the soil samples were

143 compacted in the plexiglass column using a rubber hammer. The soil column was constructed within one day. After that, the

144 soil column was allowed to stand for 3 days to obtain stable records of the hydrological sensors.

145

146 2.3 Data collection

147 In the soil column test, the following data was collected:

148 (1) Boundary conditions: rainfall intensity (r, mm/h), potential evaporation (PE, mm/h) at 1 h time interval, temperature (T, ℃)

149 and relative humidity (RH, %) at 5 min time interval.

150 (2) Hydrological data: volume water content (θ_{exp}, %) and soil matrix suction (S_{exp}, kPa) in different depths at 5 min time

151 interval, cumulative drainage from the top (D_{top}, g) and bottom (D_{bottom}, g) of the soil column.

152 (3) Crack geometric data: crack ratio ($w_{c,exp}$), crack aperture ($w_{j,exp}$), and the maximum crack depth (d_{max}, mm). The $w_{c,exp}$

153 and $w_{j,exp}$ were obtained via processing the crack photos which were taken at 20 min intervals during drying periods. The

154 image processing method mainly includes two steps as shown in Fig. 3. The d_{max} was measured by thin wire before each

155 rainfall event.
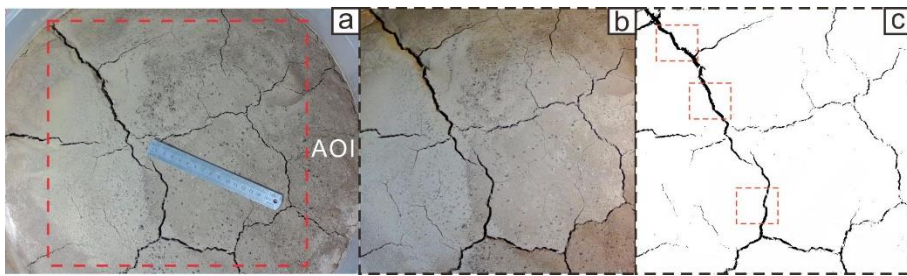
156

157 Fig. 3 Process of crack image processing. (a) a photo obtained from the HD camera, 800 pixels × 1400 pixels; (b) crack

158 image after cropping and pixel enhancement, 1044 pixels × 1005 pixels; (c) crack image after binarization and denoise, and

159 the crack ratio was calculated as the crack area divided by the overall area of interest, the crack aperture was calculated as the

160 average value of crack aperture from three different positions.

161

162 2.4 Test procedure

163 The overall experimental process included two stages of WD cycles. The purpose of the first stage was to generate a relatively

164 stable surface pattern of the desiccation cracks. It started from 2022/01/05 15:00 to 2022/02/28 9:00, including thirteen WD

165 cycles.

The second stage started from 2022/02/28 9:00 to 2022/03/28 22:30, including seven WD cycles. Fig. 4 presents the variation of rainfall, evaporation, temperature and relative humidity in the entire experiment process. Because the two warm lamps and fan were closed during the night, two kinds of evaporation intensity can be observed during the drying periods. In addition, the average environment temperature in the 5th WD cycle was higher because we turned up the power of the two warm lamps. In this current study, we mainly focus on the second stage of WD cycles.
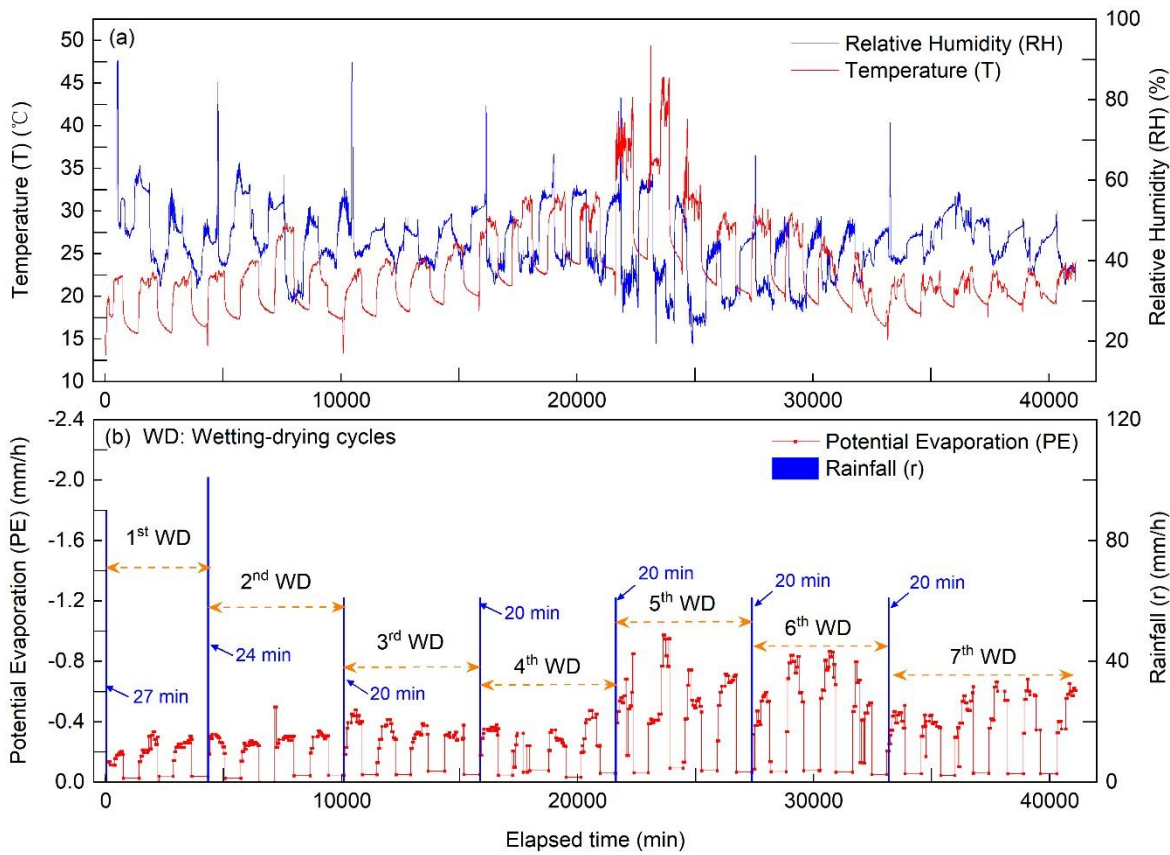
Fig. 4 Environmental conditions of the experiment. (a) time series of temperature and relative humidity; (b) rainfall intensity and potential evaporation.

3. Model Description

3.1 Dual-permeability model (DPM)

The DPM concept used in this study corresponds to the one developed by Gerke and Van Genuchten (1993a). The model divides the flow domain into two overlapping and interacting continua according to the volumetric ratios of each domain, where two coupled 2-D Richards' equations are used to describe the matrix flow and preferential flow as

$$C_c(h)\frac{\partial h_c}{\partial t}=\nabla[K_c(h)\nabla(h_c+z)]-\frac{\Gamma_w}{w_c} \qquad (1)$$

$$C_m(h)\frac{\partial h_m}{\partial t}=\nabla[K_m(h)\nabla(h_m+z)]+\frac{\Gamma_w}{w_m} \qquad (2)$$

$$\Gamma_w=\alpha_w K_a(h_c-h_m) \qquad (3)$$

$$w_c+w_m=1 \qquad (4)$$

where subscript "c" and "m" indicate the crack and matrix domains, respectively; h (m) is the pressure head; C represents the specific water capacity, $d\theta/dh$ (1/m); θ (-) is the volumetric water content; K (m/s) is the isotropic hydraulic conductivity; z (m) is the elevation head; w (-) is the volumetric ratio of the crack domain or matrix domain over the bulk soil volume; Γ_w is the water exchange term (1/s) between the two domains; α_w (1/m²) is the effective water transfer coefficient; K_a

188 (m/s) is the interface hydraulic conductivity.

189 The hydraulic properties of the two domains are parameterized based on the Mualem-van Genuchten soil-water retention

190 curves (SWRC) (Mualem, 1976; Van Genuchten, 1980) as

191 $$S_e(h) = \frac{\theta - \theta_r}{\theta_s - \theta_r} = \left[1 + (|\alpha h|)^n\right]^{-m} \qquad (5)$$

192 $$K(S_e) = K_s K_r(S_e) = K_s S_e^{0.5}[1 - (1 - S_e^{1/m})^m]^2 \qquad (6)$$

193 where S_e (-) is the effective saturation; θ_s (-) and θ_r (-) are the saturated and residual volumetric water content, respectively;

194 α (1/m), n (-) and m (-) are fitting parameters; K_s (m/s) is the saturated hydraulic conductivity; K_r (-) is the relative

195 hydraulic conductivity.

196 According to Gerke and Van Genuchten (1993a), the total porosity ε (-), total volume water content θ (-), total hydraulic

197 conductivity K (m/s) and total volumetric flux (m/s) in terms of the volume ratio of each domain can be expressed as

198 $$\varepsilon = w_c \varepsilon_c + w_m \varepsilon_m \qquad (7)$$

199 $$\theta = w_c \theta_c + w_m \theta_m \qquad (8)$$

200 $$K = w_c K_c + w_m K_m \qquad (9)$$

201 Note that the total porosity ε is define as the total pore volume (V_p) divided by total soil volume (V), while ε_m (or ε_c) is

202 defined as the pore volume in matrix ($V_{p,m}$) (or crack, $V_{p,c}$) domain divided by the volume of that domain (V_m or V_c). The total

203 volume water content has the same definition.

204 In the case of a DPM model, specified flux i is divided between the matrix and crack domains as

205 $$i = w_c i_c + w_m i_m \qquad (10)$$

206 where i_c and i_m are the effective boundary fluxes into each domain (m/s).

207 Considering a rainfall condition, the effective boundary fluxes of the two domains are initially equal to rainfall intensity (r)

208 due to the infiltration capacity of each domain is larger than r (Dusek et al., 2008), and therefore the boundary fluxes of each

209 domain can be written as

210 $$i_c = r \qquad (11)$$

211 $$i_m = r \qquad (12)$$

212 As the soil keeps wetting, the decrease of the pressure head gradient may firstly lead to the infiltration capacity of matrix

213 domain dropping to a value less than r. Then, ponding occurs on the surface of the soil matrix and the boundary condition

214 changes to a specified pressure head boundary. This transformation can be achieved in COMSOL, a multi-physic solver and

215 simulation software package building on finite element method, by using a combined type of boundary (Dirichlet and

216 Neumann) proposed by Chui and Freyberg (2009). Once ponding occurs on the matrix domain, the surplus water from that

217 domain infiltrates into the crack domain and its effective flux increases to

218 $$i_c = (r - w_m i_m) / w_c \qquad (13)$$

219 when the retained water volume in the cracks exceeds its storage capacity, water will pond on the surface of the crack domain.

220 Considering an evaporation condition, the Wilson-Fredlund-Barbour-Penman experimental function model (Wilson et al.,

221 1997) was used to calculate the actual evaporation of each domain

222 $$AE / PE = \exp\left(\frac{-Sg\omega_v}{\xi(1 - h_a)\gamma_w R(T_s + 273.15)}\right) \qquad (14)$$

223 where AE is the actual evaporation; PE is the potential evaporation measured in the experiment; S (kPa) is total matric suction

224 at the soil surface; g (m/s²) is the gravitational acceleration constant; ω_v is molecular mass of water, 0.018kg/mol; ξ is

225 a dimensional empirical parameter with a suggested value of 0.7; h_a is relative humidity of overlying air; γ_w is unit mass

226   of water, 9.807 kN/m^3; R is universal gas constant, 8.314J/(mol·K); T_s (°C) is the soil surface temperature.

227

228   3.2 Dynamic dual-permeability model (DPMDy)

229   3.2.1 Porosity description

230   In Stewart et al. (2016a); (2016b) and Stewart (2018), the total porosity (ϕ_{max}) of a cracked soil was divided into three domains:

231   aggregates (or soil matrix), cracks (voids from horizontal deformation induced by desiccation cracks) and subsidence (voids

232   from vertical deformation induced by desiccation cracks). In Stewart et al. (2016a), the distributions of these domains change

233   as a function of a unified water content, U

234    $$\phi_{max} = \phi_{matrix}(U) + \phi_{crack}(U) + \phi_{sub}(U) \qquad (15)$$

235   where the subscripts matrix, crack and sub refer to the aforementioned three domains. In this study, we assume that the

236   horizontal deformation dominates the formation of desiccation cracks, thus $\phi_{sub}(U)$ can be neglected.

237   Stewart et al. (2016a) then deduced the porosities of each domain as:

238    $$\phi_{matrix}(U) = (\phi_{max} - \phi_{min})(\frac{p+1}{p+U^{-q}}) + \phi_{min} \qquad (16)$$

239    $$\phi_{crack}(U) = (\phi_{max} - \phi_{min})(\frac{1-U^{q}}{1+pU^{q}}) \qquad (17)$$

240   where p and q are functional shape parameters; ϕ_{max} is the maximum porosity of a soil core prior to shrinkage and thus also

241   represents the total porosity; ϕ_{min} is the minimum porosity of the matrix domain; U is a unified water content (defined as

242   water content u divided by its saturated value u_{max}), which can be approximately estimated to be the saturation degree ($S_{e,m}$)

243   in an SWRC function of the soil matrix (Stewart et al., 2016a). Indeed, Eq. (16) represents a shrinkage curve function in which

244   four parameters can be obtained through a shrinkage test.

245   Substituting $S_{e,m}$ as U and incorporating Eq. (5) into Eq. (16) and Eq. (17), we can obtain the porosity of the two domains as

246   a function of pressure head h

247    $$\phi_{matrix}(h) = (\phi_{max} - \phi_{min})(\frac{p+1}{p+S_{e,m}^{-q}}) + \phi_{min} = (\phi_{max} - \phi_{min})(\frac{p+1}{p+\left(\left[1+(|\alpha_m h_m|)^{n_m}\right]^{-m_m}\right)^{-q}}) + \phi_{min} \qquad (18)$$

248    $$\phi_{crack}(h) = (\phi_{max} - \phi_{min})(\frac{1-S_{e,m}^{q}}{1+pS_{e,m}^{q}}) = (\phi_{max} - \phi_{min})(\frac{1-\left(\left[1+(|\alpha_m h_m|)^{n_m}\right]^{-m_m}\right)^{q}}{1+p\left(\left[1+(|\alpha_m h_m|)^{n_m}\right]^{-m_m}\right)^{q}}) \qquad (19)$$

249   With these porosity equations in mind, we can rewrite Eq. (4) and Eq. (7) as:

250    $$\phi_{max} = w_c \varepsilon_c + (1-w_c)\varepsilon_m \qquad (20)$$

251   Because the crack domain is mainly composed of voids, we here assume that $V_{p,c}$ equals to V_c, and thus $\varepsilon_c = 1$. Through this

252   assumption, we obtained a physically-consistent definition of how the porosity and crack volume vary as functions of

253   saturation degree as follow

254    $$w_c \varepsilon_c = w_c = \phi_{crack}(S_{e,m}) = (\phi_{max} - \phi_{min})(\frac{1-S_{e,m}^{q}}{1+pS_{e,m}^{q}}) \qquad (21)$$

255    $$\varepsilon_m = \frac{\phi_{matrix}(S_{e,m})}{1-w_c} = \left[(\phi_{max} - \phi_{min})(\frac{p+1}{p+S_{e,m}^{-q}}) + \phi_{min}\right] / \left[1-(\phi_{max} - \phi_{min})(\frac{1-S_{e,m}^{q}}{1+pS_{e,m}^{q}})\right] \qquad (22)$$

256

257   3.2.2 Water content and hydraulic conductivity

258   In terms of Eq. (8), the total water content of the soil volume can be expressed as:

259   $\theta = \phi_{crack}(h)\theta_c + (1 - \phi_{crack}(h))\theta_m$ (23)

260   Regarding the hydraulic conductivity of each domain, the classical DPM often assumed it equals to the product of a fixed K_s

261   and the relative hydraulic conductivity of the corresponding domain. The following equations are obtained according to Eq.

262   (6).

263   $K_m = K_{m,s}K_r(S_{e,m}) = K_{m,s}S_{e,m}^{0.5}[1 - (1 - S_{e,m}^{1/m_m})^{m_m}]^2$ (24)

264   $K_c = K_{c,s}K_r(S_{e,c}) = K_{c,s}S_{e,c}^{0.5}[1 - (1 - S_{e,c}^{1/m_c})^{m_c}]^2$ (25)

265   where $K_{c,s}$ and $K_{m,s}$ refer to the saturated hydraulic conductivity in crack and matrix domains, respectively.

266   However, the $K_{c,s}$ and $K_{m,s}$ are transient variables that changes with the crack geometries in crack domain and porosity in

267   matrix domain, which should be taken into consideration in a shrinking-swelling soil. To solve this issue, Stewart et al. (2016b)

268   further deduced models that describe the relationships between $K_{m,s}$, $K_{c,s}$ and $S_{e,m}$.

269   $K_{m,s}(S_{e,m}) = K_{m,\max}\left(\dfrac{p+1}{p + S_{e,m}^{-q}}\right)$ (26)

270   $K_{c,s}(S_{e,m}) = K_{c,\max}\left(\dfrac{1 - S_{e,m}^q}{1 + pS_{e,m}^q}\right)^2$ (27)

271   where $K_{c,\max}$ is the maximum saturated hydraulic conductivity of the crack domain (at $S_{e,m} = 0$) when the crack aperture

272   achieves the maximum value; $K_{m,\max}$ is the maximum saturated hydraulic conductivity of the matrix domain (at $S_{e,m} = 1$)

273   when the radius of cylindrical pores in that domain achieves the maximum value (See Eq. (25) and Eq. (27) in Stewart et al.

274   (2016b)). In the DPMDy model, we here set $K_r(S_{e,c})$ to 1 in Eq. (25). This modification means that the magnitude of K_c

275   only depends on the crack area or the saturated degree of the soil matrix domain.

276   $K_c = K_{c,s} = K_{c,s}(S_{e,m}) = K_{c,\max}\left(\dfrac{1 - S_{e,m}^q}{1 + pS_{e,m}^q}\right)^2$ (28)

277   Incorporating Eq. (26) and Eq. (27) into Eq. (9) obtains:

278   $K_s = \phi_{crack}(h)K_{c,\max}\left(\dfrac{1 - S_{e,m}^q}{1 + pS_{e,m}^q}\right)^2 + (1 - \phi_{crack}(h))K_{m,\max}\left(\dfrac{p+1}{p + S_{e,m}^{-q}}\right)$ (29)

279   Note that $K_{m,\max}$ can be obtained by laboratory-based infiltration test through a saturated soil core prior to shrinkage. Then,

280   Eq. (29) can be used to fit the $K_{c,\max}$ through the overall saturated hydraulic conductivity (measured K_s) under different

281   crack volume or ratio. Alternatively, $K_{c,\max}$ can also be approximately calculated as

282   $K_{c,\max} = \dfrac{w_{j,\max}^2 g}{12v}$ (30)

283   where $w_{j,\max}$ stands for the maximum crack aperture measured in experiment (m), g is the gravity acceleration constant

284   (m/s²), and v is the water kinematic viscosity (m²/s). This equation is a relation to the cubes of the aperture of a crack with

285   respect to the crack inner flux, which is based on the derivation of laminar flow between parallel plates for Hagen-Poiseuille

286   type of flow (Snow, 1965).

Eventually, we can simulate the hydrological process with considering the dynamic changes of desiccation cracks by incorporating Eq. (19), Eq. (21), Eq. (26), Eq. (27) and Eq. (28) into the DPM.

4. Experimental results

4.1 Crack dynamic changes

Fig 5 presents typical images of crack evolution during each WD cycle. Intuitively, it seems that the crack area and width did not show an obvious increasing trend with the WD cycles as expected. Conversely, during the 1st to 4th WD cycles, the cracks at the same moment after rainfall (Fig 5b2-4) and the final state (Fig 5c2-4) decreased significantly even though the environmental temperature (T) and the potential evaporation (PE) increased in these periods. The cracks increased significantly since the 5th WD cycle, but most of them were finer than before. Overall, cracks in the 1st WD cycle are wider than those formed in other cycles.
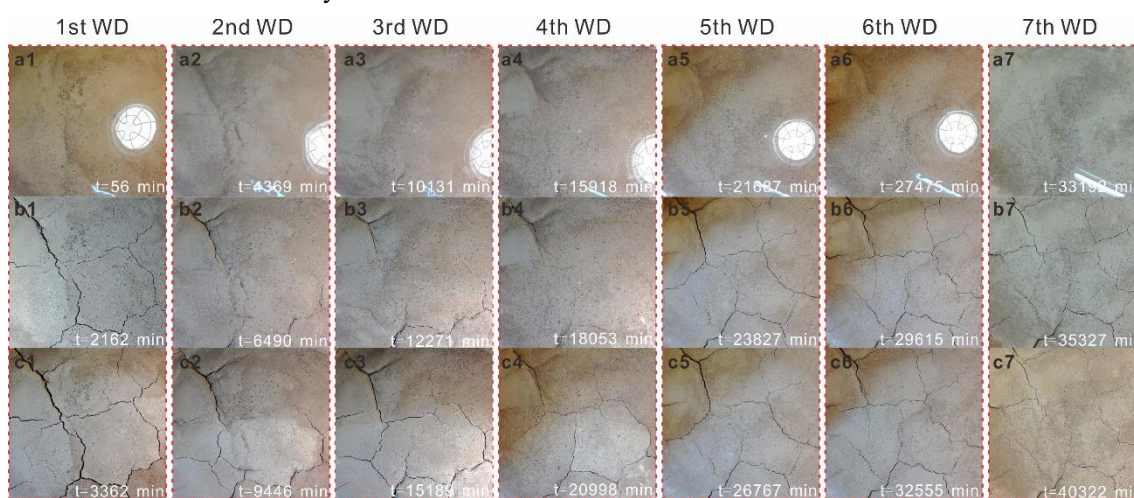
Fig. 5 Typical images of crack evolution in seven wetting-drying cycles. (a1-7) water ponds on the soil surface after rainfall; (b1-7) crack images at the 2135th min after each rainfall; (c1-7) crack images at the end of the final high evaporation period during each wetting-drying cycle

Fig 6 quantitatively shows the variation of crack ratio ($w_{c,exp}$) and crack aperture ($w_{j,exp}$) in the experiment. Overall, the variation curves corresponded to the intuitive descriptions mentioned above. Especially, an unexpected result was that the T and PE in the 5th and 6th WD cycles were higher than in previous cycles, but their maximum $w_{c,exp}$ and $w_{j,exp}$ became smaller. During a single WD cycle, the $w_{c,exp}$ and $w_{j,exp}$ have a similar trend, which shows a dramatic decrease during rainfall, rapid increase in high evaporation periods and slow increase or even decrease in low evaporation periods. More specifically, during the rainfall periods, the crack closure process was not significant until the water ponded on the soil matrix, then ponded water flowed into the cracks, leading to acceleration of the crack closure. Note that cracks were not completely closed even when they were full of water (Fig 5a1-7). The minimum crack ratio under such conditions is approximately 0.1%. In the evaporation periods, the maximum crack ratio reaches 2.87% and the maximum crack aperture reaches 2.6 mm. In addition, Fig 7 shows the maximum crack depth (d_{max}) measured after each cycle. It can be seen that d_{max} increased substantially after the 1st WD cycle and then slightly increased in the last six cycles, with a maximum value of 23.8 cm.
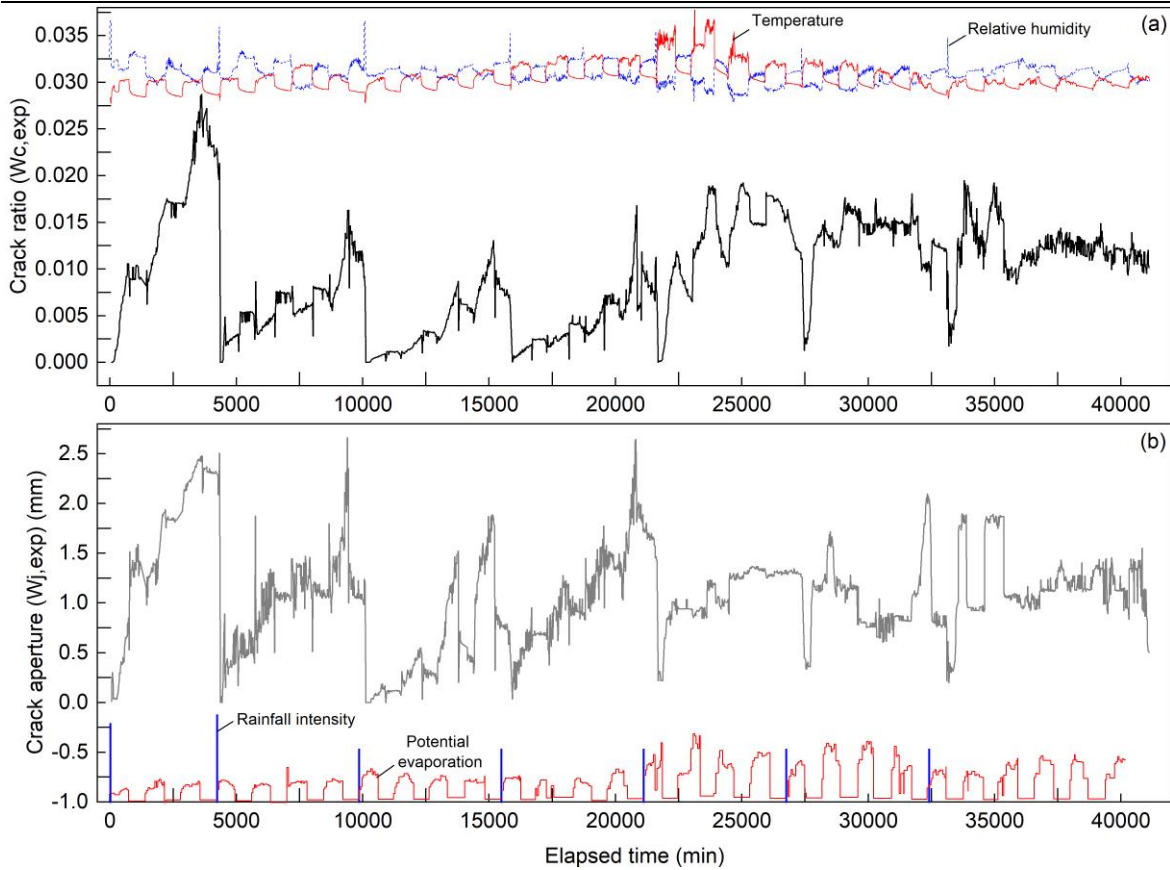
Fig. 6 Time series of crack geometries. (a) crack ratio; (b) crack aperture
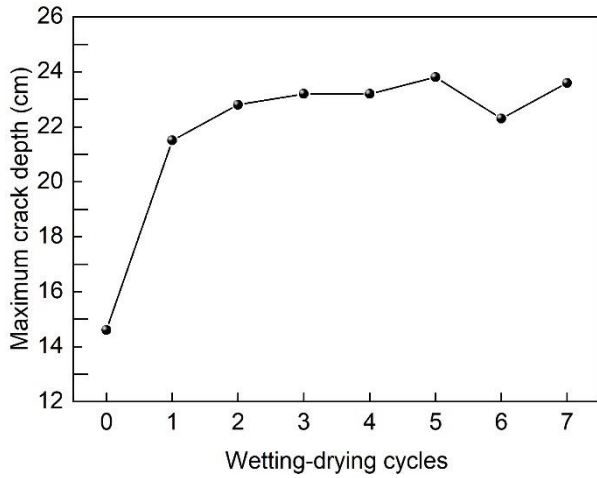
Fig. 7 The maximum crack depth measured after each wetting-drying cycle

4.2 Hydrological response

Table 2 presents the manually recorded results of external hydrological responses involving ponding and drainage during each WD cycle. It can be seen that the ponding occurred on the soil surface within 5 min after each rainfall. The ponding duration in each rainfall mainly decreased with WD cycles. Note that the ponding depth in each rainfall was below the upper drainage outlet. Regarding the water drainage, approximately 1.4 kg of water (the total water mass was 8 kg) was leaked during the 1st rainfall due to the interspace between the soil and the plexiglass column and the hydrological sensors. Then, we sealed the interspace using clay powder and polyurethane cement (soft materials without constrain effects on the soil swelling) after each drying process, and subsequently, no water drainage was observed at the bottom outlet.

Table 2 Manual readings of external hydrological responses

Wetting-drying cycles	1st	2nd	3rd	4th	5th	6th	7th
t_p (min)	4.1	1.8	1.2	1.2	1.2	2.2	2.8

Ponding duration (min)	70	160	68	47	34	25	23
Drainage (g)	1412	-	-	-	-	-	-
*t_p (min) – beginning of ponding after each rainfall							

328 Fig 8 shows the internal hydrological responses recorded by the soil moisture and water potential sensors. Because the M2

329 and M4 were damaged during soil compaction, no matric suction data was obtained at their depths. Overall, water content at

330 all depths increased during rainfall and decreased during evaporation, where T1 showed the most sensitive responses to the

331 WD cycles. During rainfall, the time for water content to respond to each rainfall increased with depths, but the time difference

332 among all depths decreased significantly since the 2nd WD cycle. During the drying periods, an interesting phenomenon was

333 that the water content at 5 cm depth showed an overall decline trend, but transient increases of water content frequently

334 appeared during low evaporation periods. Such transient increases seem to be related to the slow decrease of crack ratio as

335 mentioned in section 4.1. Regarding the matric suction, its variation trend was similar to the water content but showed more

336 delayed responses to the environmental conditions, especially in the last three WD cycles. Additionally, Fig 8b also implies

337 that soil at 5 cm depth reached saturation during each rainfall, while soil below the 25 cm depth was in the unsaturated state

338 in the whole experiment process.
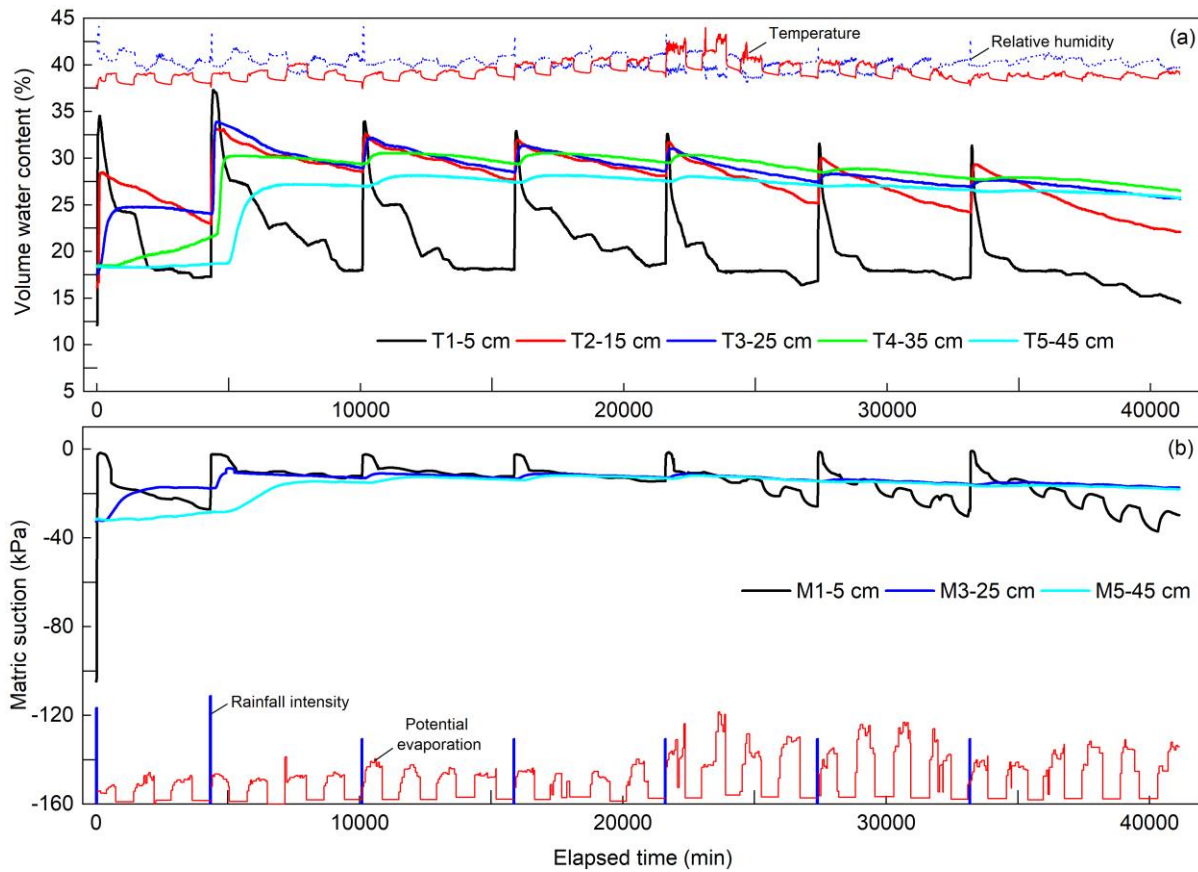
340 **Fig.8** Time series of volume water content (a) and matric suction (b) at different depths.

5. Numerical simulation

343 5.1 Set-up of numerical model

344 The single-domain model (SDM), dual-permeability model (DPM) and dynamic DPM (DPMDy) were implemented in a finite

345 element solver for Richards' equation as part of the COMSOL Multiphysics software (Comsol 5.6). As shown in Fig 9, they

346 have the same 2-D size, boundary conditions, mesh structure and initial condition. The model domain is 0.5 m by 0.5 m, same

347 as the soil column. Because the measured maximum crack depth was 23.8 cm, we specified the crack domain existing within

348 the upper 25 cm depth of the soil column.

349 The boundary conditions at the top were set as combined type of boundary conditions (as mentioned in section 3.1) for

representing the rainfall, ponding and evaporation process recorded in the experiment; the bottom side is a seepage boundary condition; the left and right sides of the model are no-flux boundaries.

Because the pressure head in the surface area may change frequently and drastically during WD cycles, a refined mesh structure with dense boundary layers was used to capture the transient hydrological conditions. The boundary layers included 15 layers of rectangular grid, with the minimum and maximum thick of approximately 0.04 cm and 0.3 cm, respectively. A coarser free-triangle mesh (average length of 1.8 cm) was defined below the boundary layers. The initial condition both in matrix and crack domains was set as the distribution of pore water pressure measured from the experiment prior to the 1st WD cycle.
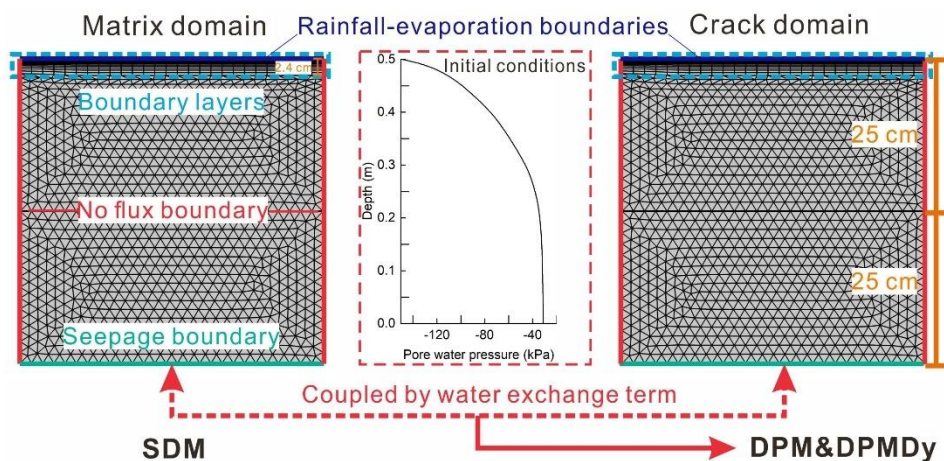
Fig. 9 Set-up of the 2-D numerical model for the SDM, DPM and DPMDy

5.2 Parameters

5.2.1 Shrinkage parameters

As shown in Fig 10, using Eq. (18) to fit the measured shrinkage curve in Fig. 2, we obtained the four shrinkage parameters as $\phi_{min}=0.22$, $\phi_{max}=0.30$, $p=8.8\pm4.84$, $q=2.71\pm0.85$. Then, the variation of porosity in crack domain (or crack ratio w_c) and matrix domain (ε_m) could be obtained using Eq. (21) and Eq. (22), respectively. Note that the minimum w_c calculated by Eq. (21) was set as 0.001 considering the incomplete closure of cracks during rainfall.
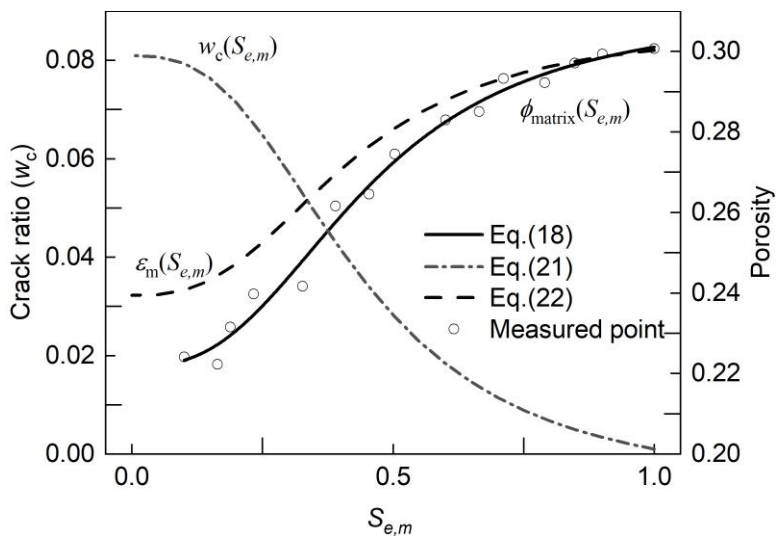
Fig. 10 Fitted shrinkage curve (solid line) and modeled porosity variation of matrix (dash line) and crack domains (dash-dot line)

5.2.2 Soil water retention parameters

Fig 11 shows the measured matric suction versus volume water content at different depths. The SWRCs were estimated using

best fitting of the van Genuchten-Mualem equation to measured soil water retention data. It can be seen that the WD cycles lead to hysteretic curves in the SWRC at 5 cm and 25 cm depths, while that at the 45 cm depth rarely show hysteretic curves. This result may also indicate that most of the cracks exist within the upper 25 cm depth of the soil column. In this study, we simply estimated an approximate single SWRC of the soil matrix through experiment data instead of incorporating the hysteretic curves into the model. For instance, the estimated SWRC curve in **Fig 11a** lies between the wetting SWRC and drying SWRC to capture the overall characteristics of wetting-drying SWRC as far as possible. Note that the shape parameter n in the upper matrix domain is slightly smaller than the lower one considering the upper soil matrix may become denser after long-time WD cycles (13 times, 54 days). Regarding the SWRC of the crack domain, as we assume the crack domain does not contain any solids, the

saturated water content ($\theta_{c,s}$) and the residual water content ($\theta_{c,s}$) of that domain was set to be 0.99 and 0.01, respectively. Meanwhile, because SWRC of the crack domain cannot be experimentally determined, we assigned the other two SWRC parameters (a=1.5 and n_c=2) to mimick coarse textured soil like behavior, and to be consistent with Poiseuille law , which implies that we neglect capillarity in the cracks.
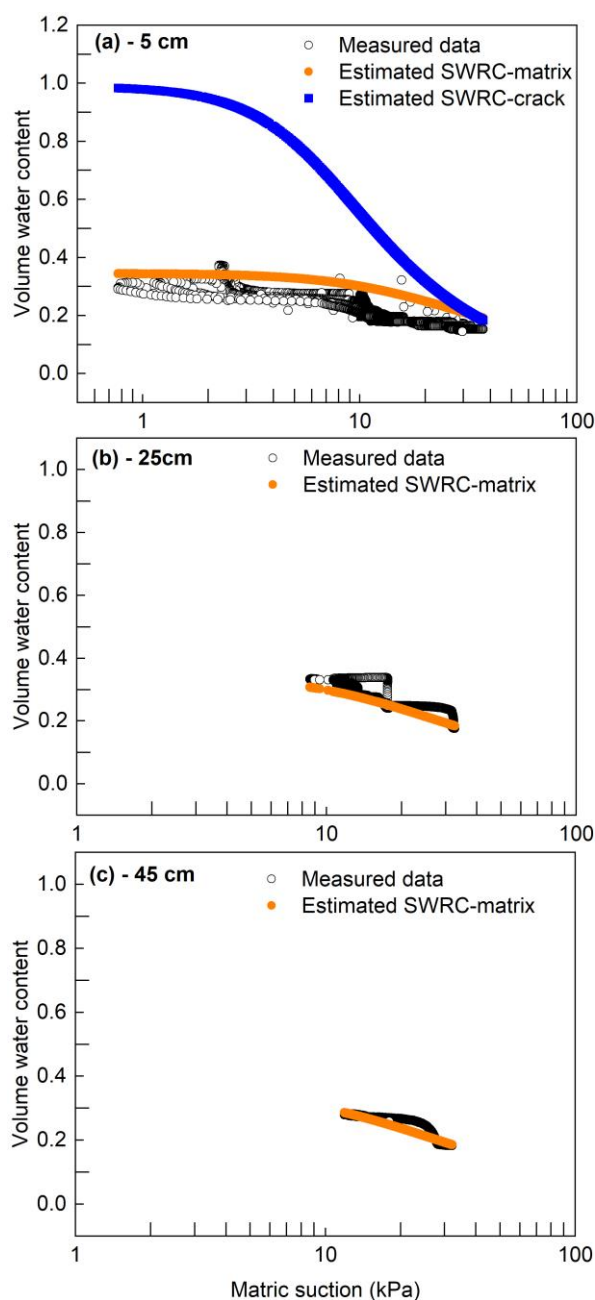
Fig. 11 Measured and estimated SWRC at different depths. (a) 5 cm; (b) 25 cm; (c) 45 cm

389   5.2.3 Hydraulic conductivity

390   As mentioned in Eq. (29), the maximum saturated hydraulic conductivity of matrix domain ($K_{m,\max}$) equals the saturated

391   hydraulic conductivity (K_s) measured in laboratory. Here, we set $K_{m,\max} = 1.16 \times 10^{-6}$ m/s. Regarding the $K_{c,\max}$, it was

392   calculated using Eq. (30), where the $w_{j,\max}$ was set to 2.6 mm obtained from Fig 6b. Then, the variation curve of transient

393   saturated hydraulic conductivity of the matrix domain ($K_{m,s}$) and the crack domain ($K_{c,s}$) could be obtained using Eq. (27)

394   and Eq. (28), respectively. Note that here we slightly modified Eq. (28) as follow.

395
$$K_{c,s}(S_{e,m}) = K_{c,\max}\left(\frac{1 - S_{e,m}{}^{q}}{1 + pS_{e,m}{}^{q}}\right)^{2} + K_{c,\min} \quad (28\text{-}b)$$

396   This modification not only avoided the $K_{c,s}$ dropping to zero thus benefits the numerical convergence, but also was

397   reasonable when considering the incomplete closure of cracks during rainfall. The $K_{c,\min}$ was also estimated using Eq. (30)

398   with a suggested $w_{j,\max} = 0.01$ mm. Further, the variation of K_m and K_c with the pressure head (h) in the DPMDy could

399   be calculated by combining Eq. (24), Eq. (26) and Eq. (28). **Fig 12** presents K_m and K_c in the three models. Note that the

400   pressure head in $K_c(h_m)$ of the DPMDy refers to that of the matrix domain (h_m), while h in $K_c(h_c)$ of the DPM refers to

401   that of the crack domain (h_c).

402

403   5.2.4 Water exchange between and pore domains

404   In the dual-permeability concept, another important parameter is the hydraulic conductivity of the interface between matrix

405   and crack domains (K_a). Generally, K_a was often estimated as the arithmetic mean of hydraulic conductivity of the two domains

406   (Arora et al., 2011; Coppola et al., 2012; 2015; Gerke and Van Genuchten, 1993b; Laine-Kaulio et al., 2014; Shao et al., 2015).

407   However, this approximation may overestimate the K_a when the hydraulic conductivity of the crack domain is much higher

408   than that of the matrix domain, especially in cracked clays. In our current study, a K_a function reformulated by (Gerke et al.,

409   2013) was adopted.

410
$$K_{a_{\min}} = \begin{cases} \min\left\{K_m(h_c), K_c(h_c)\right\} & h_c \geq h_m \\ \min\left\{K_m(h_m), K_c(h_m)\right\} & h_c < h_m \end{cases} \quad (31)$$

411   This formulation represents that the flow occurs from the highest head toward the lowest head but regulated by the less

412   permeable of the two subsystems in that instant of time (Aguilar‑López et al., 2020).

413   Regarding the α_w, experimental results presented by Song et al. (2018) showed that the saturated K_a may be 1 order of

414   magnitude larger than the $K_{m,s}$ which will represent an enlarging coefficient ranging from 10 to 18. Hence, the α_w was set

415   as 10 m^{-2} considering the saturated $K_{a_{\min}}$ determined by Eq. (31) equals to the $K_{m,s}$.

416
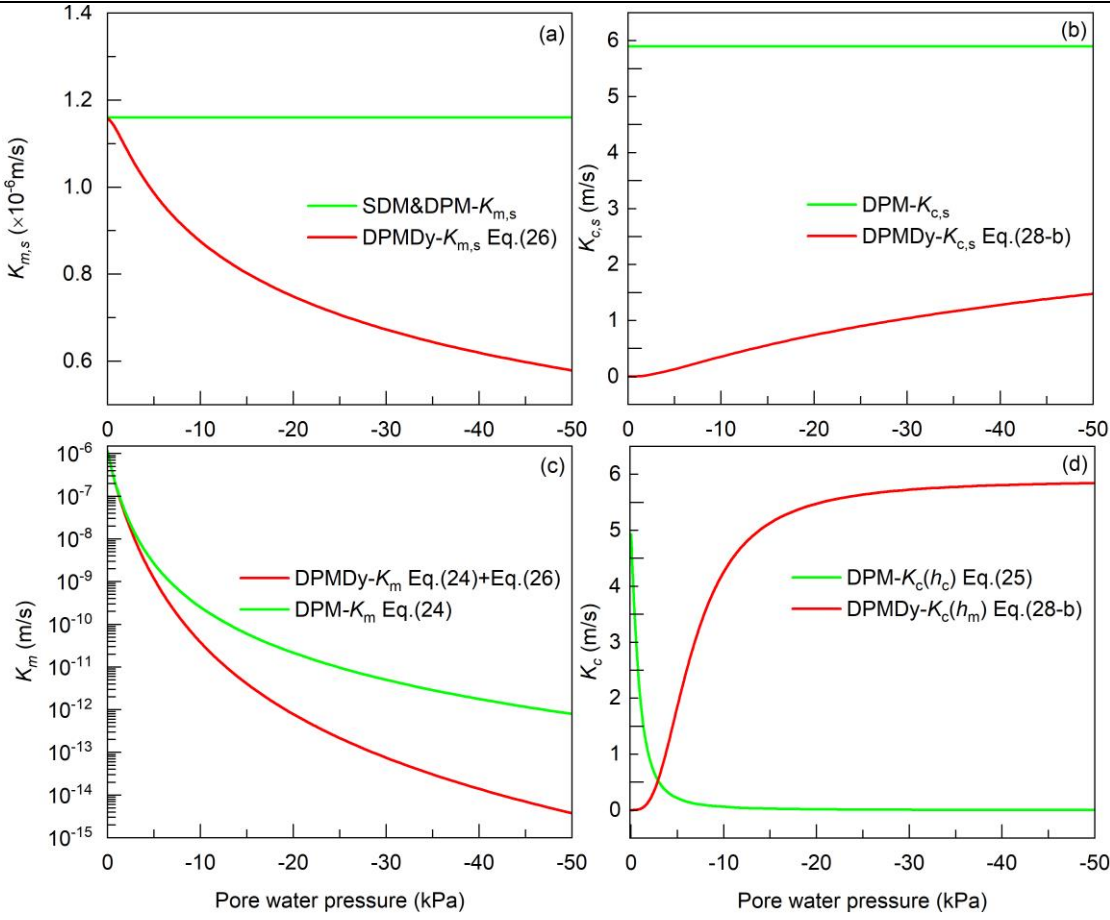
417   **Fig. 12** Modeled hydraulic conductivity of each domain in the three models. (a) Saturated hydraulic conductivity of the matrix

418   domain; (b) saturated hydraulic conductivity of the crack domain; (c) transient hydraulic conductivity of the matrix domain;

419   (d) transient hydraulic conductivity of the crack domain

420

421   All parameters and parametric methods for the SDM, DPM and DPMDy are listed in **Table 3**.

422   **Table 3** Summary of parameters and parametric methods for the SDM, DPM and DPMDy

Model	Symbol	Parameter name	Units	Upper layer	Lower layer	Parameterization
SDM DPM DPMDy	$\theta_{m,s}$	Saturated water content of matrix domain	(-)	0.345	0.345	Fitting to data
	$\theta_{m,r}$	Residual water content of matrix domain	(-)	0.01	0.01	Fitting to data
	α_m	SWRC fitting parameter of matrix domain	(1/m)	0.6	0.6	Fitting to data
	n_m	SWRC fitting parameter of matrix domain	(-)	1.65	1.8	Fitting to data
	$K_{m,max}$	The maximum K_s of matrix domain	(m/s)	1.16×10^{-6}	1.16×10^{-6}	Measured
DPM DPMDy	$\theta_{c,s}$	Saturated water content of crack domain	(-)	0.99	-	Assigned
	$\theta_{c,r}$	Residual water content of crack domain	(-)	0.01	-	Assigned
	α_c	SWRC fitting parameter of crack domain	(1/m)	1.5	-	Assigned
	n_c	SWRC fitting parameter of crack domain	(-)	2	-	Assigned
	$K_{c,max}$	The maximum K_s of crack domain	(m/s)	5.9	-	Measured
	K_a	Hydraulic conductivity of the interface	(m/s)	K_{amin}	-	Assigned
	a_w	Mass transfer coefficient	(1/m²)	10	-	Assigned
DPMDy	ϕ_{max}	The maximum porosity of a soil core	(-)	0.3	-	Fitting to data
	ϕ_{min}	The minimum porosity of a soil core	(-)	0.22	-	Fitting to data
	p	Shape parameter of soil shrinkage curve	(-)	10	-	Fitting to data
	q	Shape parameter of soil shrinkage curve	(-)	3.5	-	Fitting to data
DPM	w_c	Constant crack ratio using in DPM	(-)	0.01; 0.03	-	Assigned
* SDM: single-domain model; DPM: dual-permeability model neglecting crack dynamic changes; DPMDy: Dynamic

423

424   5.3 Simulation results

425   5.3.1 Boundary flow

426   **Fig. 13** shows the temporal evolution of the boundary flow velocity simulated by the SDM, DPM and DPMDy. As shown in

427   **Fig. 13a1 and a3**, during drying periods, the matrix domain dominates the soil evaporation process and was responsible for

428   97%-99% of the total evaporation in all the dual-permeability models. The matrix evaporation rate (e_m) simulated by the

429   DPMDy was overall lower than that of the SDM and DPM during high-intensity evaporation periods, but the crack

430   evaporation rate (e_c) simulated by the DPMDy, especially during the last three drying periods, was approximately one to two

431   orders of magnitude larger than that of the DPM (see the enlarged image in Fig. a1).

432   With regard to the wetting process, **Fig. 13a2 and a4** represent two typical infiltration patterns before and after the 5th drying

433   period (with significantly increased evaporation intensity). Overall, matrix flow still dominated the infiltration process in all

434   the dual-permeability models due to the relatively small crack ratio and depth. For the SDM, all the rainfall infiltrates into the

435   soil during the beginning of rainfall events. When the soil surface gets saturated, water ponding occured and the soil infiltration

436   rate gradually decreased. In the DPM and DPMDy, the surplus water after matrix ponding infiltrates into the crack domain as

437   preferential flow, and water will pond on the overall soil surface when the crack domain reached its storage capacity. Recall

438   that the crack volume in the DPMDy decreases with the matrix getting moist, while that in the DPM keeps constant.

439   Consequently, the ponding time of the crack domain simulated by the DPMDy in the 3nd rainfall event (inflection point of the

440   red dash line in Fig. 13a2) was 1.6 and 4.8 min earlier than that of the DPM-0.01 and DPM-0.03, respectively. The cumulative

441   preferential flow simulated by the DPMDy was 87.4% and 95.2 % less than that of the DPM-0.01 and DPM-0.03, respectively.

442   Similar rainfall pattern was obtained during the 6th rainfall event.
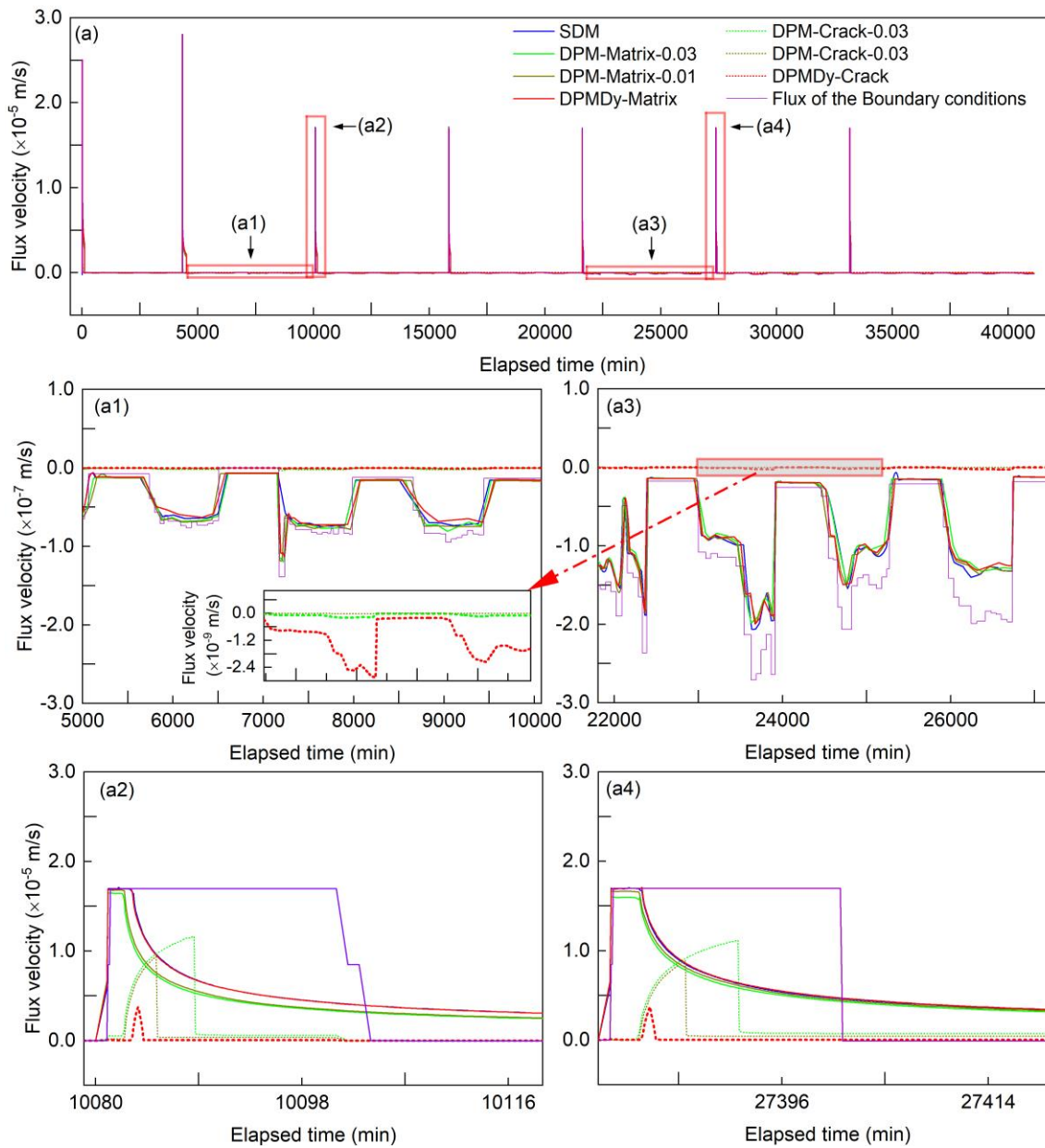
443
444 **Fig. 13** Boundary flow simulated by the SDM, DPM and DPMDy. (a) Flow velocity of the boundary conditions and simulated
445 results; (a1) and (a2) are the enlarged images of the flow velocity during the 2st drying and 3nd wetting process, respectively;
446 (a3) and (a4) are the enlarged images of the flow velocity during the 5th drying and 6th wetting process, respectively. The
447 positive value is for infiltration and negative for evaporation.

448

449 5.3.2 Water balance

450 By integrating the boundary flow velocity in Fig. 13a, the total cumulative flux for the experiment and the three models were
451 obtained (**Fig 14a**). In the experiment, the variation of water flux was estimated by calculating the sum of the difference
452 between θ_{ini} (initial volume water content) and $\theta_{t=i}$ (volume water content at any time) in the five monitoring depths.
453 Meanwhile, the water evaporation during water ponding was also estimated and added to the total flux volume. Regarding
454 the numerical model, the water balance was obtained by integrating all flow components along the upper and lower boundaries.
455 The steep increase stage of each curve represents cumulative input water flux during wetting periods and the gradual decrease
456 stage represents cumulative output water flux during drying periods. To evaluate the performance of each model on the water
457 balance, the measured cumulative input and output water fluxes in each wetting and drying stage were compared to the
458 simulated ones (Fig. 14b).
459 In Fig. 14a, the results show that the total infiltration ($I_{t,inf}$) and evaporation flux ($E_{t,eva}$) estimated from measured θ_{exp} were

460   171 mm and 138.95 mm, respectively. The $I_{t,inf}$ was 5.86 % less than the supplied water (183.44 mm) due to the water leakage.

461   The $E_{t,eva}$ was 16.48 % less than the cumulative PE (166.36 mm) because of the limit of the soil actual evaporation. Regarding

462   the simulation results, the coefficient of determination (R^2) and intercept were used to evaluate the errors made by the three

463   models. As shown in Fig. 14b, the slope of each fitting curve was fixed as 1. The SDM and DPMDy have relatively smaller

464   intercepts and slightly higher R^2 than that of the DPM-0.01 and DPM-0.03, indicative of a better coincidence to the measured

465   data. Overall, the errors in water balance caused by the three models were acceptable in this study.

466
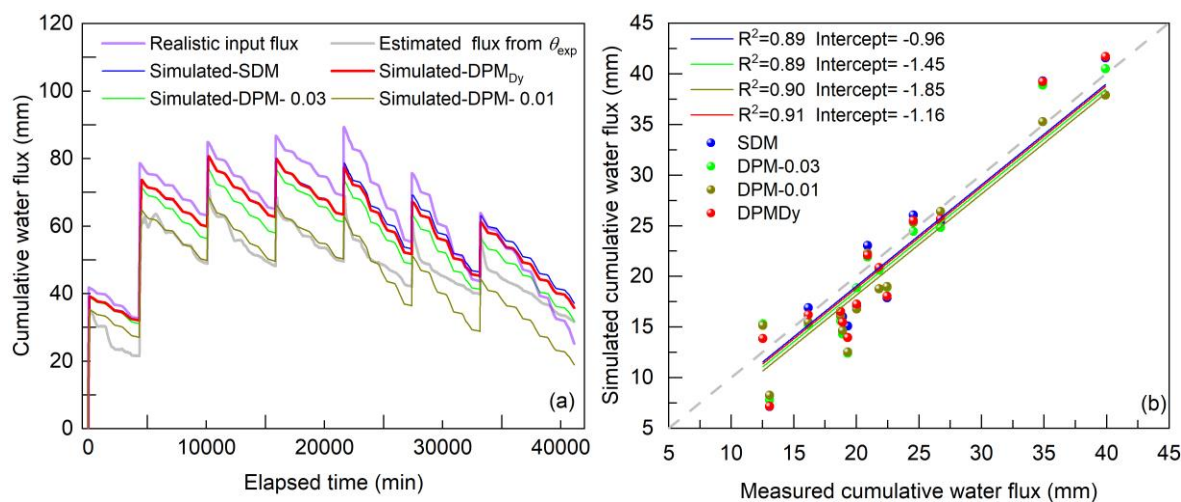
467   **Fig. 14**. Water balance for the measured and simulated results (a) Temporal evolution of total water flux calculated from the

468   measured water content, SDM, DPM and DPMDy; (b) measured versus modeled cumulative flux during each drying and

469   wetting stage

470

471   5.3.3 Crack dynamic changes and hydrological response

472   **Fig. 15** shows part of the comparison results between the measured data and the three models. Detailed descriptions of all the

473   comparison results are presented in **Appendix A**. Overall, all models show similar response trends with the measured data.

474   Divergences among the three models mainly appeared during drying.

475   In **Fig. 15a**, the simulated surficial $w_{c,sim}$ was not only generally close to the $w_{c,exp}$ in value and trend, but also it captured

476   the transient slow decrease of $w_{c,exp}$ during low evaporation periods. Notably, significant overprediction appeared in the 6th

477   and 7th wetting-drying cycles.

478   In **Fig. 15b**, the matric suction (S_{sim}) at the 25 cm depth simulated by SDM and DPMDy was close to each other and had an

479   average divergence 2.26 kPa to the measured data. The S_{sim} simulated by DPM had a greater average divergence of 3.4 kPa

480   to the measured data. They showed systematic underprediction compared to the S_{sim} simulated by SDM and DPMDy, but

481   their differences became smaller with the increasing WD cycles.

482   In **Fig. 15c**, the total volumetric water content θ_{sim} simulated by SDM was much lower with respect to the DPMDy and

483   DPM. The θ_{sim} simulated by DPM-0.01 and DPM-0.03 overpredicted the volumetric water content. The DPMDy provided

484   better prediction results but also showed slight underprediction to the measured data at the last two WD cycles.
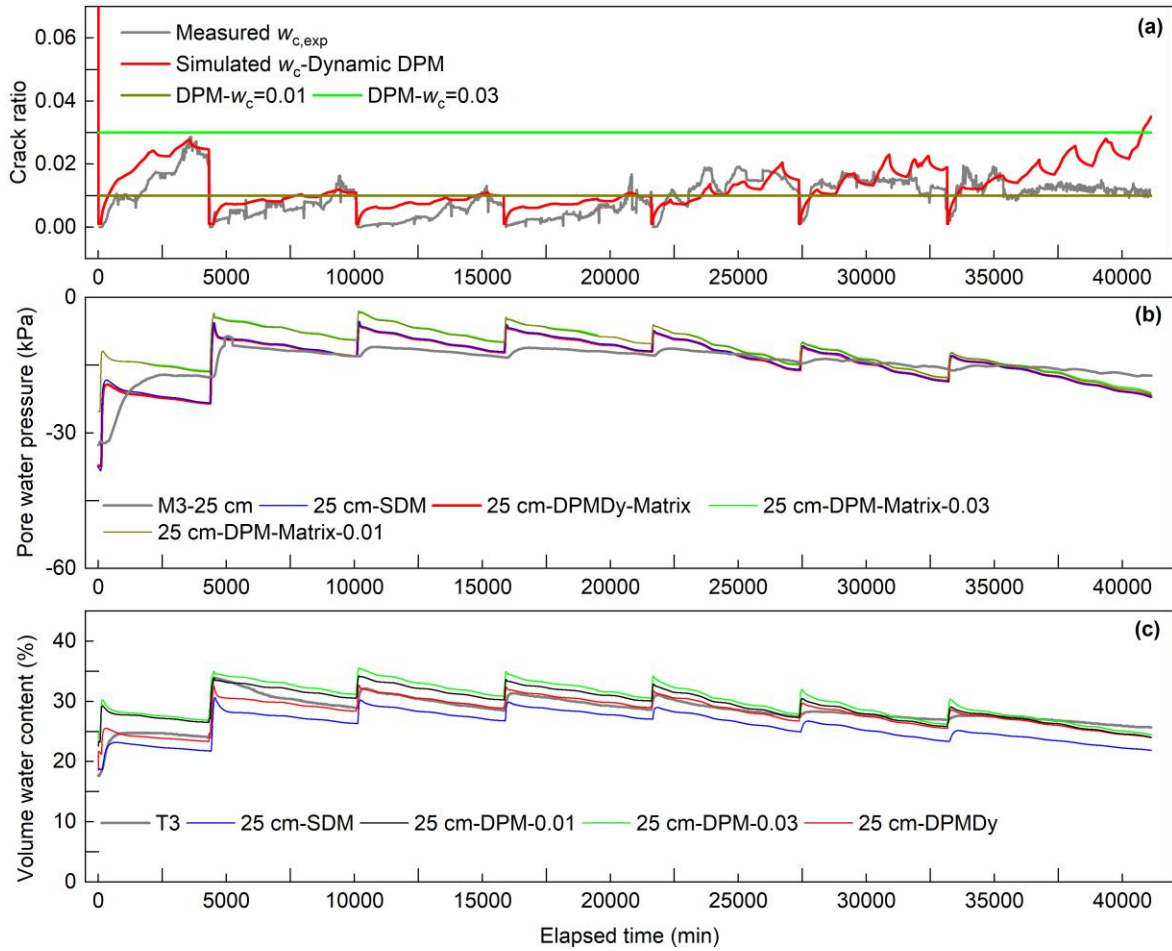
Fig. 15 Temporal evolution of the measured and simulated crack ratio, matric suction and volumetric water content. (a) Measured and simulated crack ratio on soil surface; (b) Measured and simulated matric suction at 25 cm depth; (c) Measured and simulated total water content at 25 cm depth

6. Discussions

6.1 Crack dynamic changes

Our experimental results demonstrated that the crack evolution is not always positively correlated to the increase of the WD cycles, T and PE. For instance, the 5 cm θ_{exp} at the end of the final three WD cycles was lower than that in the 1st WD cycle due to the increased T and PE, but the maximum $w_{c,exp}$ measured during the final three WD cycles was much less than that in the 1st WD cycle. From the energy-driven perspective, soil cracking and propagation can be regarded as a process that the shrinkage energy (or stress), built up from the evaporation and thermal radiation, was released until a critical moment when the tensile strength of soil is reached (Peron et al., 2009; Xu et al., 2022; Tian et al., 2022). If the environmental condition changes in a stable range, the desiccation cracks will vary within the crack pattern and the maximum $w_{j,exp}$ that were formed under the maximum shrinkage energy. In this case, new desiccation cracks will not appear in the remained soil matrix during WD cycles (**Fig 5b1-b4**). One reason is that the shrinkage energy can be fully released via previous cracks. The other reason is that the shrinkage energy is not high enough to split the soil matrix that has a denser structure (or higher tensile strength) than its initial state prior to shrinkage (Luo et al., 2021). However, once the evaporation rate and thermal radiation increase to exceed the stable range, higher shrinkage energy will lead to new cracks appearing in the soil matrix that will concurrently restrain the width increase of the previous cracks (Wang et al., 2018; Xu et al., 2021). This is the reason that cracks in the final three WD cycles are finer than the first four WD cycles. Our model describes the crack evolution mainly from the hydrological-driven perspective that assumed the surface crack pattern has become stable after undergoing 13 WD cycles and has a constant function relationship with the water content. Indeed, this assumption is reasonable for natural soils under atmospheric environmental conditions. However, our experiment not only used reconstituted soil but also intensely changed

508 the environmental conditions since the 5th WD cycle. Therefore, the model overpredicted $w_{c,exp}$ at the end of the 6th and 7th
509 WD cycles.

510 In addition, another interesting phenomenon is the transient decrease of $w_{c,exp}$ and increase of θ_{exp} measured at 5 cm depth
511 during low evaporation periods, which we called as 'self-closure' process. In light of **Fig 6** and **Fig 8**, the self-closure process
512 appeared always accompanied by relatively high *RH*. From the insight of the experiment, it is natural and common to infer
513 that the moist air wetted the surface soil from top to bottom, resulting in the self-closure phenomenon. Interestingly, our model
514 does not incorporate the vapor flow into the boundary conditions, and also the evaporation boundary only involves the outflow
515 of water, but it still managed to captured the self-closure process. **Fig 16** shows the crack images at t = 3702 and 4327 min as
516 well as the corresponding cloud chart of θ_{sim}. It can be seen that the soil surface became moist during the low evaporation
517 period, which is a typical external phenomenon reflecting the self-closure process. The simulation results show that θ_{sim}
518 near the surface soil increased during evaporation while θ_{sim} at deep soils decreased, indicative of evaporation inducing the
519 deep water move up and wet the surface soil from bottom to top. We further found that the process occurred because the water
520 flow driven by the soil water potential gradients, existing between the wet and dry soil layers, overcame the gravity. Indeed,
521 this kind of 'hydraulic lift' process frequently occurs in planted soils where root zone soil can force water flow from moist
522 deep soil layers to dry shallow soil layers (Richards and Caldwell, 1987; Bauerle et al., 2008), but was rarely reported in
523 homogeneous bare soil. We infer that the evaporation boundary conditions using Eq. (14) might play a positive role in leading
524 water move up and constraining it within the surficial soil depths when the evaporation intensity decreased. In any case, our
525 results provide an additional possible explanation to the self-closure phenomenon. Further quantitative analysis based on gas-
526 liquid two phase flow model is needed to compare the contribution of 'hydraulic lift' and moist air to the self-closure process
527 of cracks.
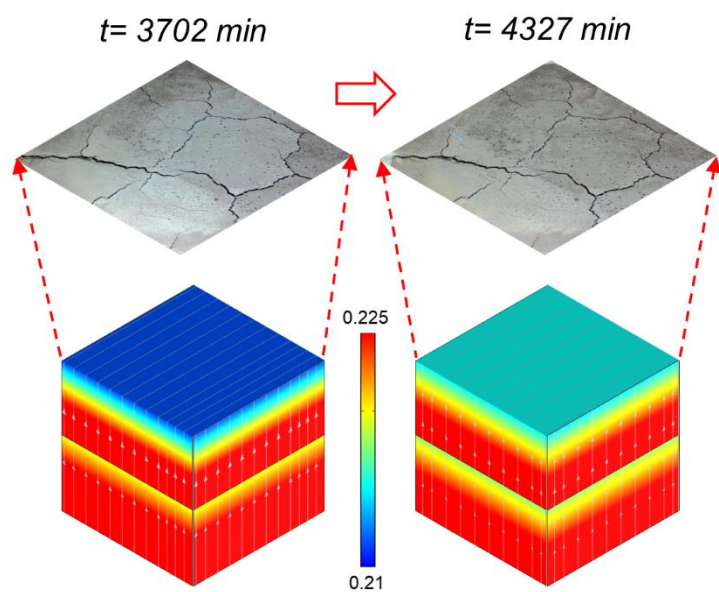
528
529 **Fig. 16** Crack images at t = 3702 and 4327 min (Photo at the top of the figures) as well as the vertical distribution of water
530 content in the numerical model (Lower part of the figures) during the low evaporation process. The left part is at the beginning
531 of the final low evaporation stage during the 1st drying periods, while the right part is at the end of the final low evaporation
532 stage during the 1st drying periods.

533
534 6.2 Water flow with dynamic changes of desiccation cracks
535 6.2.1 Water fluxes
536 As mentioned in section 5.3.1, during the drying process, the matrix and crack evaporation simulated by the DPMDy are
537 overall lower and higher than other models, respectively. It can be explained by looking at the variation of boundary K_m and

K_c in each model. Take the time span in **Fig.13a2** as an example, because the DPMDy considers the effects of matrix shrinkage on the K_m using Eq. (26), the $K_{m,DPMDy}$ is always approximately 20% and 30% lower than that of the SDM and DPM, respectively **(Fig. 17a)**. On the contrary, because the DPM links the K_c with the saturation degree of the crack domain (see Eq. (25)), the $K_{c,DPM}$ is destined to decrease with the decreased saturation degree of the crack domain induced by drying, while the $K_{c,DPMDy}$ increases with the crack development induced by drying in light of Eq. (28-b). The ultimate $K_{c,DPMDy}$ is 80% higher than the $K_{c,DPM}$ **(Fig. 17b)**. Indeed, the decrease of K_c with the drying process is an unrealistic and physically-unreasonable results. We can image that after long-term drought, the $K_{c,DPM}$ will decline to nearly zero according to Fig. 12d, which will greatly underestimate the propagation of the PF-DC in the subsequent storm event. However, many laboratory and field experiments have observed that heavy rainfall following a long-term drought facilitated PF-DC (Baram et al., 2012a; 2013; Greve et al., 2010; Kurtzman and Scanlon, 2011; Schlögl et al., 2022). By contrast, the DPMDy has the potential to capture this process for its increasing K_c with the enlarging desiccation crack during the long-term drought. In this study, because the experiment scale (or crack volume) is small, the increment of PF-DC simulated by the DPMDy after high-intensity evaporation is not significant (despite increment = 25%), but we believe the DPMDy will have a better performance in a larger scale (i.e slope scale).
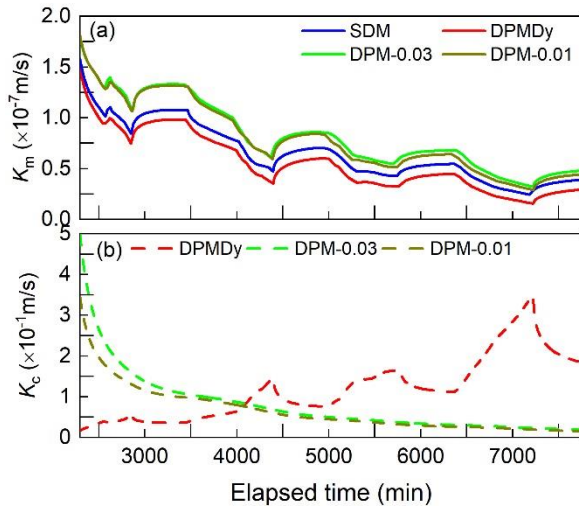
Fig. 17 Variation of boundary K_m and K_c in each model during the 5th drying periods. (a) K_m; (b) K_c

6.2.2 Water exchange and distribution

For the dual-permeability model, the two domains are coupled by the water exchange term (Eq. 3) that is governed by the pressure head difference between the two domains ($\Delta h = h_c - h_m$), water exchange coefficient (α_w) and the hydraulic conductivity between the two domains (K_a). The higher the Γ_w, the quicker the two domains equilibrate. Generally, the higher Γ_w leads to faster water exchange from the crack domain into the matrix domain and thus boosts the contribution of preferential flow on the water distribution in the soil matrix. According to the previous studies, the commonly used magnitude of the product of saturated $\alpha_w K_a$ in clay soils ranges from 10^{-5} m^{-1}s^{-1}(Aguilar‑López et al., 2020) to 10^{-6} m^{-1}s^{-1} (Coppola et al., 2012; 2015; Gerke and Maximilian Köhne, 2004; Vogel et al., 2000). In this study, the saturated $\alpha_w K_a$ is 1.16×10^{-5} m^{-1}s^{-1}, which falls in the reasonable range. Building on the above statement, the Δh and water exchange rates (Γ_w / w_m) for both the DPM and DPMDy at the 5 cm, 15 cm and 25 cm depths during the 6th rainfall event are graphed in **Fig. 18**.

As shown in **Fig. 18a1-a3**, Δh at all depths simulated by both the DPM and DPMDy rapidly reaches a positive peak value and gradually decreases with the rainfall process. The rapidly increasing positive value is because the crack domain gets

567 saturation earlier than the surrounding soil matrix due to the influx of preferential flow and the small crack storage space in

568 this study. The decrease of the Δh is ascribed to the increase of h_m with water exchanging from crack to matrix domain.

569 Notably, the crack closure process during rainfall process leads to decrease of crack volume (or crack water storage space),

570 the 'water table' (saturated zone) in the shrinking cracks elevates faster than that in the constant larger crack volume, which

571 means the h_c simulated by DPMDy is higher than the DPM-0.01 and DPM-0.03. Consequently, the time for Δh reaching

572 the peak value simulated by the DPMDy is the earliest at all the three depths, then followed by the DPM-0.01 and DPM-0.03.

573 The Γ_w / w_m simulated by the DPMDy shows the similar trend to the Δh **(Fig. 18b1-b3)**. During the 6th rainfall event, its

574 cumulative Γ_w / w_m at the 5 cm, 15 cm and 25 cm depths is (26%, 50%), (10%, 26%) and (3%, 14%) larger than that of the

575 DPM-0.01 and DPM-0.03, respectively.

576 This result means that the crack closure during wetting benefits the building-up process of the pressure head in the crack

577 domain and thus can promote water exchange from crack into matrix domain. It corresponds to some experimental results

578 that the PF-DC also exists and leads water to rapidly infiltrate into soils even if desiccation cracks are nearly closed (Baram

579 et al., 2012a; Greve et al., 2010; Luo et al., 2021; Sander and Gerke, 2007; Tuong et al., 1996). It also means using DPM may

580 overestimate the flux of PF-DC, but underestimate the water exchange coming from the PF-DC. Because the experimental

581 scale, crack ratio and depth in this study is small, the difference of simulation result involving the matric suction and water

582 content between the DPM and DPMDy is not very significant. However, we can image that the deviation caused by the DPM

583 at a larger scale will be more significant, especially in a typical shrinking-swelling soil slope under long-term WD cycles.
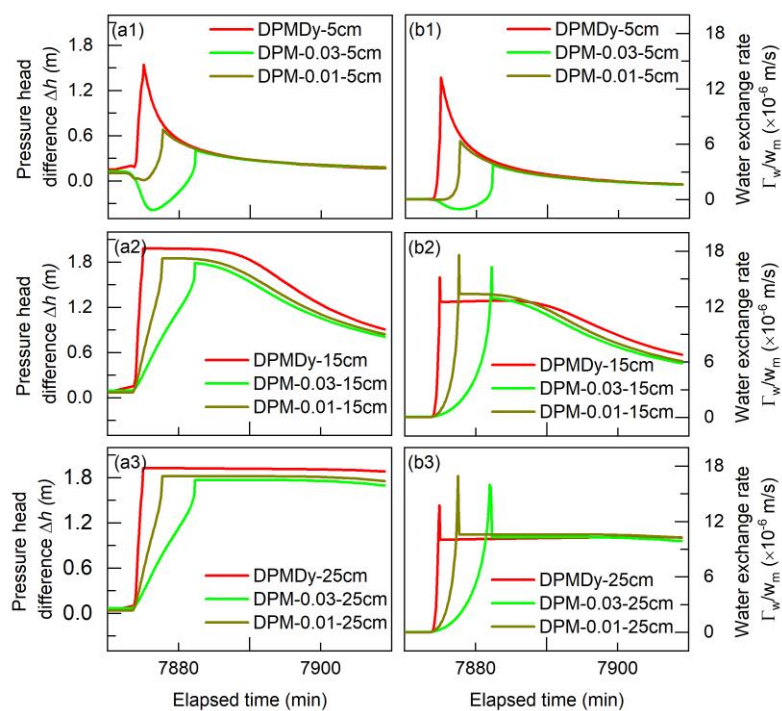
584

585 **Fig. 18** Pressure head difference (a1-a3) and water exchange rate (b1-b3) between the two domains at the 5 cm, 15 cm and

586 25 cm depths during the 6th rainfall event. The positive value of water exchange rate is for the water flowing from the crack

587 to the matrix domain, while the negative value for the opposite direction

588

589 6.3 Model performance

590 We evaluated the prediction errors of different models to the measured matric suction, water content and crack ratio using a

591 fixed slope line as the same in section 5.3.2 (see Fig. A3 and Table 4). Overall, the DPMDy, which incorporates the dynamic

592 changes of desiccation cracks and hydraulic conductivity into the dual-permeability model, has an overall better performance

593 than the SDM and DPM, as indicated by small intercept and high R^2. With regard to the water flux, while the three models all

594 give a good fit with the measured data, the DPM overpredicted the water flux of PF-DC but underestimated the water exchange

from cracks to soil matrix compared to other models. It implies that adopting a constant crack volume in the DPM model, whether it is an average or a maximum value of the measured crack ratio, will overestimate the PF-DC, which may be unsuitable to evaluate the irrigation efficiency. With regard to the matric suction (or pore water pressure), although the SDM has good performance as the DPMDy does, it significantly underpredicted the volume water content and thus may overestimate landslide stability in a moisture-content-dependent threshold method. Further, we expect that the SDM may show much poorer performance if one applies it to scenarios where the cracks are deeper and the soil has a higher swelling-shrinking ability than that of our experiment. A comprehensive model sensitivity analysis will be conducted in our future work.

Table 4 Summary of fitting performance of different models to measured data

Models	SDM		DPMDy			DPM-0.03		DPM-0.01	
Prediction variables	S	θ	S	θ	w_c	S	θ	S	θ
Slope	1								
Confidence interval	95%								
Intercept	1.51	-1.88	1.35	0.45	1.02	3.91	2.19	3.74	1.79
R^2	0.34	0.53	0.38	0.50	0.47	-0.05	0.21	-0.03	0.13

Compared to other dynamic preferential flow models, the DPMDy developed in this study also has its unique advantages. Firstly, the variation of crack volume (or crack ratio) in our model is deduced from the changes of matrix porosity due to shrinkage and thus has a universal definition. Instead, Coppola et al. (2012); (2015) linked the crack ratio to the suction head with an empirical natural logarithm function, which is not transferable to other types of soils. Secondly, a common defect in classical DPMs is that they often set the hydraulic conductivity of the crack domain (K_c) varies as a function of the saturated degree calculated from the SWRC of the crack domain (i.e Eq. (25)). This will lead to an unreasonable extremely low K_c in drying initial conditions (Aguilar‑López et al., 2020). In our model, we set the relative hydraulic conductivity of the crack domain to unit (K_r =1). It ensures that the magnitude of K_c only depends on the crack area or the saturated degree of the soil matrix domain, which provides a potential solution for remedying the shortcoming mentioned above. Thirdly, compared to some dynamic preferential flow models neglecting the water exchange between the two domains (Jamalinia et al., 2020; Kroes et al., 2000; Luo et al., 2021; Stewart, 2018) or that ones adopting an arithmetic mean of hydraulic conductivity of the two domains (Coppola et al., 2012; 2015; Laine-Kaulio et al., 2014; Shao et al., 2018) that tends to overestimate the water exchange, our model tentatively adopts an improved exchange term proposed by Gerke et al. (2013), which we showed to be a logical and satisfactory improvement in simulating water exchange in our experiment.

However, in the current study, the hysteresis effect was neglected in both the soil deformation and SWRC because we assumed the soil shrinking-swelling behavior has less influence on the pore-size distribution (or SWRC shape) but more influence on the porosity (or hydraulic conductivity). This assumption inevitably caused some errors when compared to the measured water content, especially for the surficial soil layer that has been significantly affected by the WD cycles. Our future work will try to incorporate the hysteresis effect into the current model to further improve the prediction strength. Besides, we have to remind again that because the shrinking-swelling model in our method is developed based on the hydrological-driven perspective, it may be more suitable in the natural soil layer where the crack pattern already has a stable state after long-term WD cycles.

7. Conclusions

This study combined an experimental study and a numerical simulation to quantify the preferential flow induced by dynamic changes of desiccation cracks (PF-DC). A soil column infiltration test under wetting-drying conditions was conducted to investigate dynamic changes of desiccation cracks and the accompanying water infiltration process. The variation of crack geometry, including crack ratio, width and depth were measured. The soil volumetric water content, matric suction and water

drainage were also monitored. A new dynamic dual-permeability model (DPMDy) was developed to account for the PF-DC, which includes physically-consistent functions in describing the variation of both porosity and hydraulic conductivity in crack and matrix domains. The performance of the single-domain model (SDM), rigid dual-permeability model (DPM) and DPMDy was evaluated by comparing their simulation results to the monitoring data.

Overall, the DPMDy performed not only better prediction on the crack evolution and hydrological response with respect to the SDM and DPM, but also provided much better descriptions on the underlying physics involving the PF-DC. During the drying periods, the matrix evaporation modeled by the DPMDy is lower than that of the SDM and DPM due to considering the permeability decay induced by soil shrinkage. But the crack evaporation modelled in the DPMDy approach is the highest because it managed to capture the raised crack permeability induced by drying-enlarging desiccation cracks. Compared to the DPM with fixed crack volume, the DPMDy revealed that the crack closure process during wetting will lead to a faster pressure head building-up process in the crack domain and higher water exchange rates from the crack to the matrix domain. Additionally, using a fixed crack ratio in the DPM, whether it is the maximum or the average value from the experiment data, will overestimate the infiltration fluxes of PF-DC but underestimate its contribution to the matrix domain.

The DPMDy developed here has a physically-consistent definition. It remedies the shortcomings of the RDPM and other dynamic preferential flow models in defining the dynamic changes of desiccation cracks and hydraulic properties of the crack domain and interface. Future works should focus on considering the hysteresis effect of the SWRC curve during wetting-drying cycles in the model and its application to complex field situations.

Appendix A

Fig. A1 and **Fig. A2** show the temporal evolution of the measured and simulated crack ratio on the soil surface, matric suction (negative pore water pressure) and volumetric water contents at the five monitoring depths (5, 15, 25, 35 and 45 cm).

In **Fig A1a**, the simulated $w_{c,sim}$ was not only generally close to the $w_{c,exp}$ in value and trend, but also it captured the transient slow decrease of $w_{c,exp}$ during low evaporation periods.

In **Fig A1b-f**, the matric suction (S_{sim}) simulated by SDM and DPMDy is close to each other and has average divergence of 2.75 kPa, 2.26 kPa and 5.02kPa to the measured data at the 5 cm, 25 cm and 45 cm depths, respectively. The S_{sim} simulated by DPM has a greater average divergence of 2.78 kPa, 3.4 kPa and 7.43 kPa to the measured data at the three corresponding depths.

In **Fig A2a-e**, the volumetric water content θ_{sim} simulated by SDM was much lower than that simulated by DPMDy and DPM. In most depths (except the 5 cm and 45 cm depth), SDM systematically underpredicted the volumetric water content during both wetting and drying periods. By contrast, the θ_{sim} simulated by DPM-0.01 and DPM-0.03 overpredicted the volumetric water content. The DPMDy gave overall better prediction results in most depths, but has significant divergences to the measured data at the depth of 5 cm and so are the other two models.
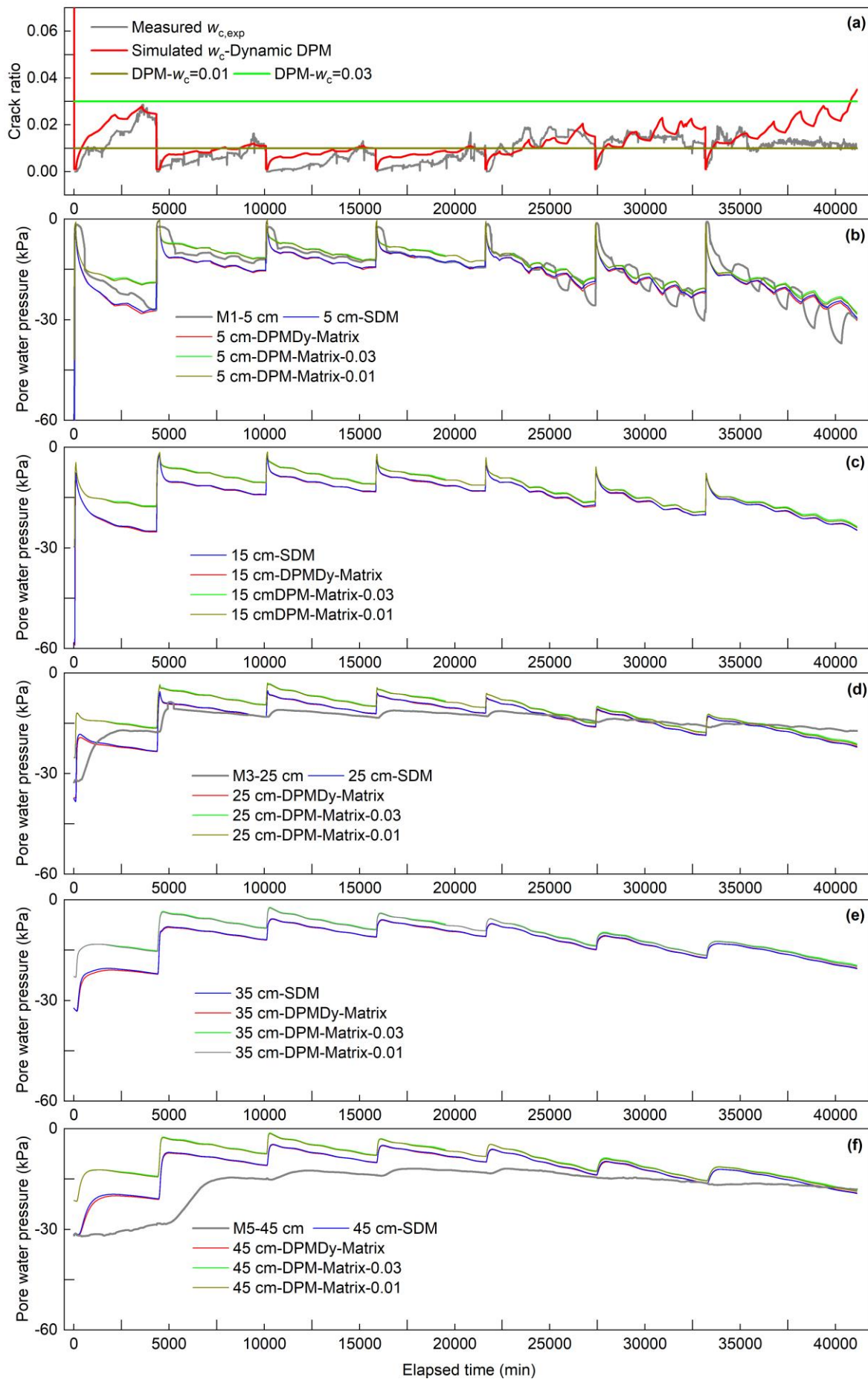
Fig. A1 Temporal evolution of the measured and simulated crack ratio and matric suction at different depths. (a) Measured and simulated crack ratio (Dynamic DPM) on soil surface; (b-f) Measured and simulated matric suction (Single domain model, DPM and Dynamic DPM) at depths of 5 cm, 15 cm, 25 cm, 35 cm and 45 cm.
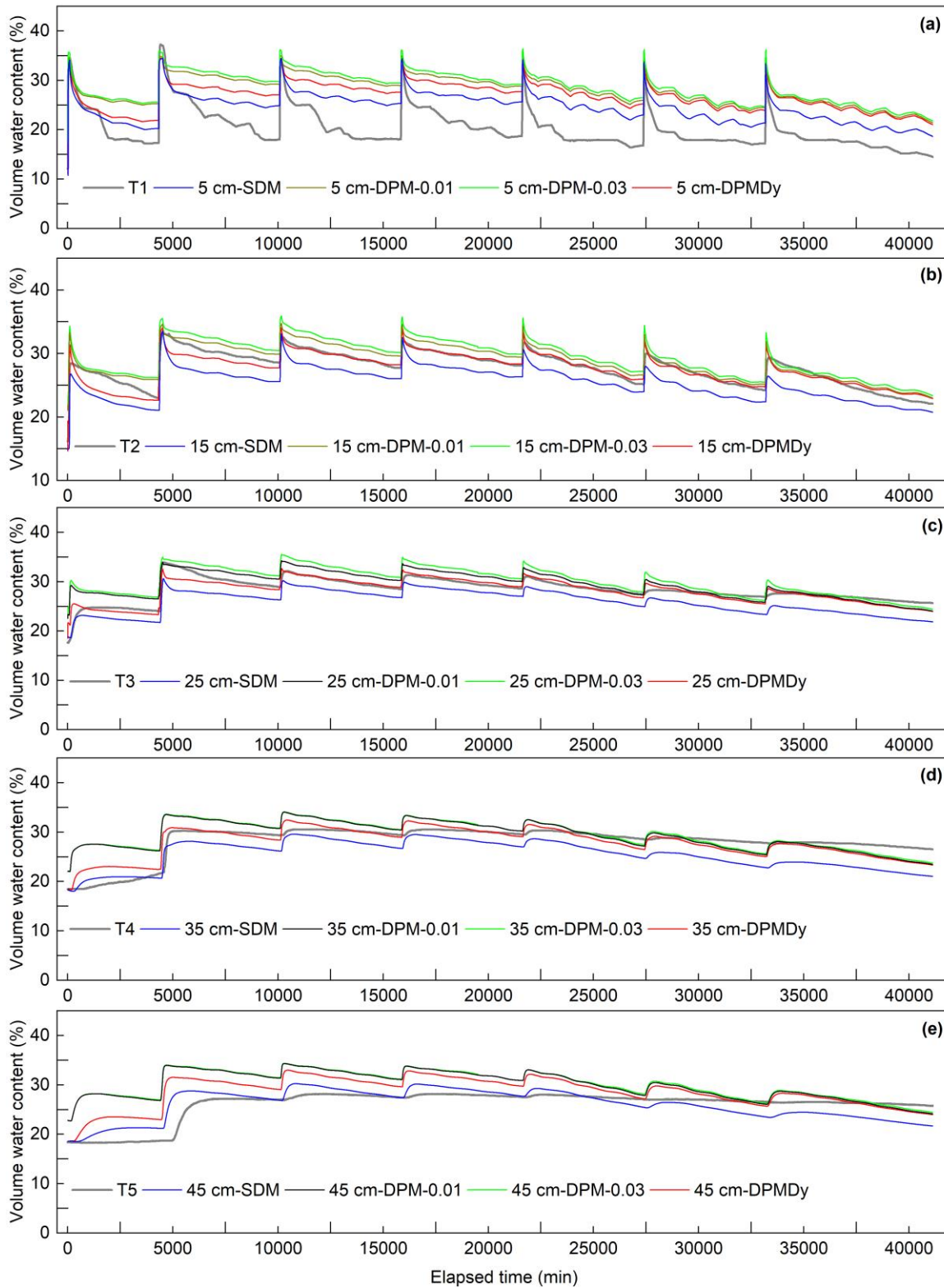
668
669 **Fig. A2** Temporal evolution of the measured and simulated volumetric water content at depths of 5 cm, 15 cm, 25 cm, 35 cm
670 and 45 cm. Note that the simulated volumetric water content demonstrated here is the total volumetric water content that
671 combined with the combined matrix and crack domains using Eq. (8)
672

673
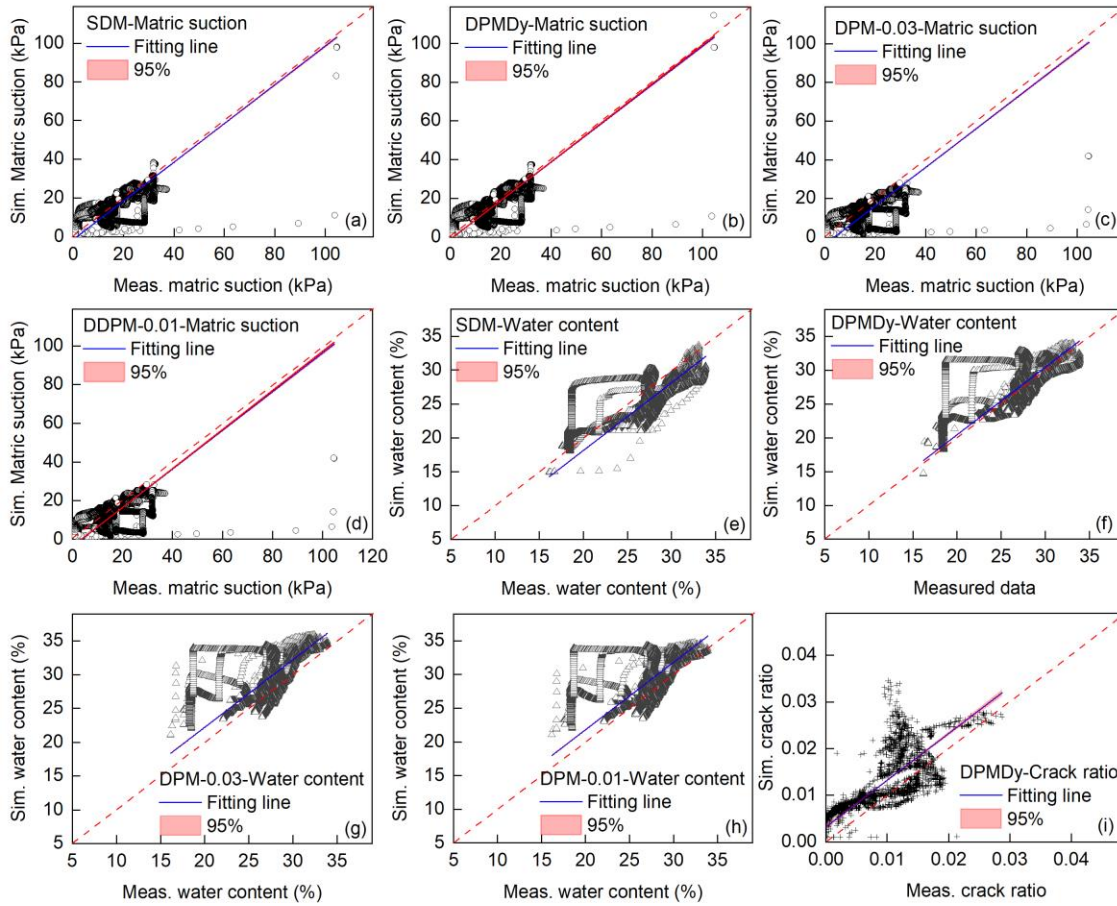
674 Fig A3 Scatter plots of modeled vs measured data. (a), (b), (c) and (d) refer to the matric suction simulated by SDM, DPMDy,

675 DPM-0.03 and DPM-0.01, respectively; (e), (f), (g) and (h) refer to the volumetric water content simulated by SDM, DPMDy,

676 DPM-0.03 and DPM-0.01, respectively; (i) crack ratio simulated by DPMDy. Sim. means simulated and Meas. means

677 measured.

678

679 **Notation**

PF-DC	Preferential flow induced by desiccation cracks
SDM	Single-domain model
EMs	Explicit crack models
DPoM	Dual-porosity model
DPM	Rigid dual-permeability model with fixed crack ratio and hydraulic conductivity
DPM-0.01	Rigid dual-permeability model with crack ratio of 0.01
DPM-0.03	Rigid dual-permeability model with crack ratio of 0.03
DPMDy	Dynamic DPM with changing crack ratio and hydraulic conductivity
WD cycles	Wetting-drying cycles

θ	Total water content (combined matrix and crack domains), m^3m^{-3}
θ_{exp}	Volumetric water content measured in the experiment, m^3m^{-3}
θ_m	Volumetric water content of the matrix domain, m^3m^{-3}
θ_c	Volumetric water content of the crack domain, m^3m^{-3}
$\theta_{m,s}$	Saturated volumetric water content of the matrix domain, m^3m^{-3}
$\theta_{m,r}$	Residual volumetric water content of the matrix domain, m^3m^{-3}
$\theta_{c,s}$	Saturated volumetric water content of the crack domain, m^3m^{-3}
$\theta_{c,r}$	Residual volumetric water content of the crack domain, m^3m^{-3}

$S_{e,m}$	Saturation degree of the matrix domain, m³m⁻³
$S_{e,c}$	Saturation degree of the crack domain, m³m⁻³
α_m	Parameter for the van Genuchten water retention curve of the matrix domain, 1/m
n_m	Parameter for the van Genuchten water retention curve of the matrix domain, 1/m
m_m	Parameter for the van Genuchten water retention curve of the matrix domain, 1/m
α_c	Parameter for the van Genuchten water retention curve of the crack domain, 1/m
n_c	Parameter for the van Genuchten water retention curve of the crack domain, 1/m
m_c	Parameter for the van Genuchten water retention curve of the crack domain, 1/m
h_m	Pressure head of the matrix domain, m
h_c	Pressure head of the crack domain, m
C_c	Specific water capacity of the crack domain which is defined as $d\theta_c / dh_c$, 1/m
C_m	Specific water capacity of the matrix domain which is defined as $d\theta_m / dh_m$, 1/m
K_s	Total transient saturated hydraulic conductivity of the soil (combined matrix and crack domains), m/s
K_c	Transient hydraulic conductivity of the crack domain, m/s
$K_{c,s}$	Saturated hydraulic conductivity of the crack domain, m/s
$K_{c,max}$	The maximum crack hydraulic conductivity when the crack reaches its maximum crack aperture, m/s
$K_{c,min}$	The minimum crack hydraulic conductivity when the crack reaches its minimum crack aperture, m/s
$K_{c,r}$	Relative hydraulic conductivity of the crack domain, m³m⁻³
K_m	Transient hydraulic conductivity of the matrix domain, m/s
$K_{m,s}$	Saturated hydraulic conductivity of the matrix domain, m/s
$K_{m,max}$	The maximum matrix hydraulic conductivity prior to soil shrinkage, m/s
$K_{m,r}$	Relative hydraulic conductivity of the matrix domain, m³m⁻³
K_a	Hydraulic conductivity between the matrix and crack domains, m/s
$K_{a_{min}}$	An improved hydraulic conductivity between the matrix and crack domains reformulated by Gerke et al. (2013), m/s
Γ_w	Water exchange term between the crack and matrix domains, 1/s
w_c	Crack ratio, which is defined as volumetric ratio between the crack domain and the overall soil volume, m³m⁻³
$w_{c,exp}$	Surface crack ratio measured in experiment, m²m⁻²
$w_{j,exp}$	Average crack aperture (or crack width) measured in the experiment, m
$w_{j,max}$	The maximum average crack aperture measured in the experiment, m
d_{max}	The maximum crack depth measured in the experiment, m
w_m	Volumetric ratio between the matrix domain and the overall soil volume, m³m⁻³
α_w	Effective water transfer coefficient, 1/m²
V	Total soil volume (combined matrix and crack domains), m³
V_m	Volume of the soil matrix domain, m³
V_c	Volume of the crack domain, m³
V_p	Total pore volume, m³
$V_{p,m}$	Pore volume in the matrix domain, m³
$V_{p,c}$	Pore volume in the crack domain, m³
ε	Total soil porosity (combined matrix and crack domains), which is defined as V_p/V, m³m⁻³
ε_m	Effective porosity of the matrix domain, which is defined as $V_{p,m}/V_m$
ε_c	Effective porosity of the crack domain, which is defined as $V_{p,c}/V_c$
i	Total effective infiltration rate (combined matrix and crack domains), m/s
i_m	Effective infiltration rate of the matrix domain, m/s

i_c	Effective infiltration rate of the crack domain, m/s
e_m	Effective evaporation rate of the matrix domain, m/s
e_c	Effective evaporation rate of the crack domain, m/s
r	Rainfall intensity, m/s
AE	Actual evaporation rate, m/s
PE	Potential evaporation rate, m/s
S	Total matric suction at the soil surface, kPa
S_{exp}	Soil matric suction measured in the experiment, kPa
g	Gravitational acceleration constant, m/s^2
ω_v	Molecular mass of water, kg/mol
ξ	Dimensional empirical parameter with a suggested value of 0.7
h_a	Relative humidity of soil overlying air
γ_w	Unit mass of water, kN/m^3
R	Universal gas constant, J/mol·K
T_s	Soil surface temperature, °C
ϕ_{max}	Total porosity (or the maximum porosity) of a soil core prior to soil shrinkage, which is defined as V_p/V and thus equals to the ε , m^{3}m^{-3}
ϕ_{min}	The minimum porosity of the matrix domain, m^{3}m^{-3}
ϕ_{matrix}	Porosity of the matrix domain, which is defined as $V_{p,m}/V$, m^{3}m^{-3}
ϕ_{crack}	Porosity of the crack domain, which is defined as $V_{p,c}/(V_m+V_c)$, m^{3}m^{-3}
ϕ_{sub}	Porosity of the subsidence zone, which is defined as voids induced by soil subsidence divided by the total soil volume, m^{3}m^{-3}
U	A unified water content, which is defined as the gravimetric water content u divided by its saturated value u_{max}
p	Functional shape parameters of the soil shrinkage curve
q	Functional shape parameters of the soil shrinkage curve
v	Water kinematic viscosity, m^2/s
t_P	Beginning of ponding time after each rainfall, min
Δh	Pressure difference between the crack and matrix domains, which is defined as $h_c - h_m$

680

Code/Data availability

682 The source code and the data generated from this study are available from the corresponding author upon reasonable request.

683

Author contribution

685 Yi Luo: Conceptualization, Methodology, Investigation, Writing-original draft preparation

686 Jiaming Zhang*: Supervision, Writing - review & editing, Project administration

687 Zhi Zhou: Resources, Software, Investigation

688 Juan P. Aguilar-Lopez: Writing - review & editing

689 Roberto Greco: Writing - review & editing

690 Thom Bogaard: Supervision, Writing - review & editing, Funding acquisition

691

Competing interests

693 Some authors are members of the editorial board of journal Hydrology and Earth System Sciences. The peer-review process

694 was guided by an independent editor, and the authors have also no other competing interests to declare.

695

Financial support

This work was financially supported by the National Natural Science Foundation of China (42177166) and the Fundamental Research Funds for National University, China University of Geosciences (Wuhan). It was also partially funded by the Plan of Anhui Province Transport Technology Progress (grant 2018030) and Engineering Research Center of Rock-Soil Drilling & Excavation and Protection, Ministry of Education (202210).

Acknowledgment

This paper was written during visiting research exchange of Yi Luo at TUDelft in Summer 2022. The experiment was conducted from January to March 2022 in China, Professor Ming-jian Hu and his research group are thanked for their great help in providing TDR probes. Yi Luo's Chinese colleagues Yuhao Li, Zhan Yang, Xiang Li, Zijian Shen are thanked for their contribution on the experiment monitoring. The authors also would like to thank the editor and anonymous reviewers for their valuable comments that substantially improved this paper.

References

Aguilar‑López, J. P., Bogaard, T. A., and Gerke, H. H.: Dual‑Permeability Model Improvements for Representation of Preferential Flow in Fractured Clays, Water Resour. Res., 56, 10.1029/2020wr027304, 2020.

Arora, B., Mohanty, B. P., and McGuire, J. T.: Inverse estimation of parameters for multidomain flow models in soil columns with different macropore densities, Water Resour Res, 47, 2010WR009451, 10.1029/2010WR009451, 2011.

Baram, S., Kurtzman, D., and Dahan, O.: Water percolation through a clayey vadose zone, J. Hydrol., 424-425, 165-171, 10.1016/j.jhydrol.2011.12.040, 2012a.

Baram, S., Ronen, Z., Kurtzman, D., Külls, C., and Dahan, O.: Desiccation-crack-induced salinization in deep clay sediment, Hydrol. Earth Syst. Sci., 17, 1533-1545, 10.5194/hess-17-1533-2013, 2013.

Bauerle, T. L., Richards, J. H., Smart, D. R., and Eissenstat, D. M.: Importance of internal hydraulic redistribution for prolonging the lifespan of roots in dry soil, Plant Cell Environ, 31, 177-186, 10.1111/j.1365-3040.2007.01749.x, 2008.

Bogaard, T. A. and Greco, R.: Landslide hydrology: from hydrology to pore pressure, WIREs Water, 3, 439-459, 10.1002/wat2.1126, 2015.

Caris, J. P. T. and Van Asch, T. W. J.: Geophysical, geotechnical and hydrological investigations of a small landslide in the French Alps, Eng. Geol., 31, 249-276, 10.1016/0013-7952(1)90011-9, 1991.

Chaduvula, U., Viswanadham, B. V. S., and Kodikara, J.: Centrifuge model studies on desiccation cracking behaviour of fiber-reinforced expansive clay, Geotext. Geomembr., 50, 480-497, 10.1016/j.geotexmem.2022.02.001, 2022.

Chen, C., Roseberg, R. J., and Selker, J. S.: Using microsprinkler irrigation to reduce leaching in a shrink/swell clay soil, Agric. Water Manage., 54, 159-171, 10.1016/s0378-3774(01)00150-0, 2002.

Cheng, Q., Tang, C.-S., Xu, D., Zeng, H., and Shi, B.: Water infiltration in a cracked soil considering effect of drying-wetting cycles, J. Hydrol., 593, 10.1016/j.jhydrol.2020.125640, 2021.

Chui, T. F. M. and Freyberg, D. L.: Implementing Hydrologic Boundary Conditions in a Multiphysics Model, J. Hydrol. Eng., 14, 1374-1377, 10.1061/(asce)he.1943-5584.0000113, 2009.

Coppola, A., Comegna, A., Dragonetti, G., Gerke, H. H., and Basile, A.: Simulated Preferential Water Flow and Solute Transport in Shrinking Soils, Vadose Zone J., 14, 10.2136/vzj2015.02.0021, 2015.

Coppola, A., Gerke, H. H., Comegna, A., Basile, A., and Comegna, V.: Dual-permeability model for flow in shrinking soil with dominant horizontal deformation, Water Resour. Res., 48, 10.1029/2011wr011376, 2012.

Davidson, M. R.: A Green-Ampt Model of infiltration in a cracked soil, Water Resour. Res., 20, 1685-1690, 10.1029/WR020i011p01685, 1984.

Dusek, J., Gerke, H. H., and Vogel, T.: Surface Boundary Conditions in Two-Dimensional Dual-Permeability Modeling of Tile Drain Bromide Leaching, Vadose Zone J., 7, 1287-1301, 10.2136/vzj2007.0175, 2008.

Favre, F., Boivin, P., and Wopereis, M. C. S.: Water movement and soil swelling in a dry, cracked Vertisol, Geoderma, 78, 113-123, 10.1016/s0016-7061(97)00030-x, 1997.

Gerke, H. H. and Maximilian Köhne, J.: Dual-permeability modeling of preferential bromide leaching from a tile-drained glacial till agricultural field, J. Hydrol., 289, 239-257, 10.1016/j.jhydrol.2003.11.019, 2004.

Gerke, H. H. and van Genuchten, M. T.: A dual-porosity model for simulating the preferential movement of water and solutes in structured porous media, Water Resour. Res., 29, 305-319, 10.1029/92wr02339, 1993a.

Gerke, H. H. and van Genuchten, M. T.: Evaluation of a first-order water transfer term for variably saturated dual-porosity flow models, Water Resour. Res., 29, 1225-1238, 10.1029/92wr02467, 1993b.

Gerke, H. H., Dusek, J., and Vogel, T.: Solute Mass Transfer Effects in Two-Dimensional Dual-Permeability Modeling of Bromide Leaching From a Tile-Drained Field, Vadose Zone J., 12, 10.2136/vzj2012.0091, 2013.

Germann, P. F. and Karlen, M.: Viscous-Flow Approach to In Situ Infiltration and In Vitro Saturated Hydraulic Conductivity Determination, Vadose Zone J., 15, 10.2136/vzj2015.05.0065, 2016.

Greco, R.: Preferential flow in macroporous swelling soil with internal catchment: model development and applications, J. Hydrol., 269, 150-168, 10.1016/s0022-1694(02)00215-9, 2002.

Greve, A., Andersen, M. S., and Acworth, R. I.: Investigations of soil cracking and preferential flow in a weighing lysimeter filled with cracking clay soil, J. Hydrol., 393, 105-113, 10.1016/j.jhydrol.2010.03.007, 2010.

Hendrickx., J. M. H. and Flury, M.: Conceptual Models of Flow and Transport in the Fractured Vadose Zone, in: Panel on Conceptual Models of Flow and Transport in the Fractured Vadose Zone, National Academy Press, Washington D.C., 149-187, 2001.

Jamalinia, E., Vardon, P. J., and Steele-Dunne, S. C.: The impact of evaporation induced cracks and precipitation on temporal slope stability, Comput. Geotech., 122, 10.1016/j.compgeo.2020.103506, 2020.

Jarvis, N., Koestel, J., and Larsbo, M.: Understanding Preferential Flow in the Vadose Zone: Recent Advances and Future Prospects, Vadose Zone J., 15, 10.2136/vzj2016.09.0075, 2016.

Khan, M. S., Hossain, S., Ahmed, A., and Faysal, M.: Investigation of a shallow slope failure on expansive clay in Texas, Eng. Geol., 219, 118-129, 10.1016/j.enggeo.2016.10.004, 2017.

Krisnanto, S., Rahardjo, H., Fredlund, D. G., and Leong, E. C.: Water content of soil matrix during lateral water flow through cracked soil, Eng. Geol., 210, 168-179, 10.1016/j.enggeo.2016.06.012, 2016.

Kroes, J. G., Wesseling, J. G., and Van Dam, J. C.: Integrated modelling of the soil – water – atmosphere – plantsystem using the model SWAP 2.0 an overview of theory andan application, Hydrol. Processes, 14, 10, https://doi.org/10.1002/1099-1085(20000815/30)14:11/12<1993::AID-HYP50>3.0.CO;2-%23, 2000.

Kurtzman, D. and Scanlon, B. R.: Groundwater Recharge through Vertisols: Irrigated Cropland vs. Natural Land, Israel, Vadose Zone J., 10, 662-674, 10.2136/vzj2010.0109, 2011.

Laine-Kaulio, H., Backnäs, S., Karvonen, T., Koivusalo, H., and McDonnell, J. J.: Lateral subsurface stormflow and solute transport in a forested hillslope: A combined measurement and modeling approach, Water Resour. Res., 50, 8159-8178, 10.1002/2014wr015381, 2014.

Larsbo, M. and Jarvis, N. J.: MACRO5.0. A model of water flow and solute transport in macroporous soil. Technical description, 2003.

Lepore, B. J., Morgan, C. L. S., Norman, J. M., and Molling, C. C.: A Mesopore and Matrix infiltration model based on soil structure, Geoderma, 152, 301-313, 10.1016/j.geoderma.2009.06.016, 2009.

Liu, C.-W., Cheng, S.-W., Yu, W.-S., and Chen, S.-K.: Water infiltration rate in cracked paddy soil, Geoderma, 117, 169-181, 10.1016/s0016-7061(03)00165-4, 2003.

Luo, Y., Zhang, J.-m., Zhou, Z., Shen, Z.-j., Chong, L., and Victor, C.: Investigation and prediction of water infiltration process in cracked soils based on a full-scale model test, Geoderma, 400, 10.1016/j.geoderma.2021.115111, 2021.

Mooney, S. J. and Morris, C.: A morphological approach to understanding preferential flow using image analysis with dye tracers and X-ray Computed Tomography, Catena, 73, 204-211, 10.1016/j.catena.2007.09.003, 2008.

Mualem, Y.: A new model for predicting the hydraulic conductivity of unsaturated porous media, Water Resour. Res., 12, 513-522, 10.1029/WR012i003p00513, 1976.

Nimmo, J. R.: Theory for Source-Responsive and Free-Surface Film Modeling of Unsaturated Flow, Vadose Zone J., 9, 295-306, 10.2136/vzj2009.0085, 2010.

Nimmo, J. R., Perkins, K. S., Plampin, M. R., Walvoord, M. A., Ebel, B. A., and Mirus, B. B.: Rapid-Response Unsaturated Zone Hydrology: Small-Scale Data, Small-Scale Theory, Big Problems, Front. Earth Sci., 9, 10.3389/feart.2021.613564, 2021.

Pei, P., Zhao, Y., Ni, P., and Mei, G.: A protective measure for expansive soil slopes based on moisture content control, Eng. Geol., 269, 10.1016/j.enggeo.2020.105527, 2020.

Peron, H., Hueckel, T., Laloui, L., and Hu, L. B.: Fundamentals of desiccation cracking of fine-grained soils: experimental characterisation and mechanisms identification, Canadian Geotechnical Journal, 46, 1177-1201, 10.1139/t09-054, 2009.

Richards, J. H. and Caldwell, M. M.: Hydraulic lift: Substantial nocturnal water transport between soil layers by Artemisia tridentata roots, Oecologia, 73, 486-489, 10.1007/BF00379405, 1987.

Sander, T. and Gerke, H. H.: Preferential Flow Patterns in Paddy Fields Using a Dye Tracer, Vadose Zone J., 6, 105-115, 10.2136/vzj2006.0035, 2007.

Schlögl, J., Wimmer, B., Cramaro, L., Wirsching, J., Poll, C., Pagel, H., Kandeler, E., Huhn, C., Griebler, C., Stumpp, C., and Haderlein, S. B.: Heavy rainfall following a summer drought stimulates soil redox dynamics and facilitates rapid and deep

800   translocation of glyphosate in floodplain soils, Environ Sci Process Impacts, 24, 825-838, 10.1039/d1em00527h, 2022.

801   Shao, W., Bogaard, T. A., Bakker, M., and Greco, R.: Quantification of the influence of preferential flow on slope stability using a

802   numerical modelling approach, Hydrol. Earth Syst. Sci., 19, 2197-2212, 10.5194/hess-19-2197-2015, 2015.

803   Shao, W., Yang, Z., Ni, J., Su, Y., Nie, W., and Ma, X.: Comparison of single- and dual-permeability models in simulating the

804   unsaturated hydro-mechanical behavior in a rainfall-triggered landslide, Landslides, 15, 2449-2464, 10.1007/s10346-018-1059-0,

805   2018.

806   Šimůnek, J., Jarvis, N. J., van Genuchten, M. T., and Gärdenäs, A.: Review and comparison of models for describing non-equilibrium

807   and preferential flow and transport in the vadose zone, J. Hydrol., 272, 14-35, 10.1016/s0022-1694(02)00252-4, 2003.

808   Smith, R. J., Raine, S. R., and Minkevich, J.: Irrigation application efficiency and deep drainage potential under surface irrigated

809   cotton, Agric. Water Manage., 71, 117-130, 10.1016/j.agwat.2004.07.008, 2005.

810   SNOW, D. T.: A parallel plate model of fractured permeable media, University of California, Berkeley ProQuest Dissertations

811   Publishing1965.

812   Song, L., Li, J., Garg, A., and Mei, G.: Experimental study on water exchange between crack and clay matrix, Geomech. Eng., 14,

813   9, https://doi.org/10.12989/gae.2018.14.3.283, 2018.

814   Stewart, R. D.: A Dynamic Multidomain Green-Ampt Infiltration Model, Water Resour. Res., 54, 6844-6859,

815   10.1029/2018wr023297, 2018.

816   Stewart, R. D.: A Generalized Analytical Solution for Preferential Infiltration and Wetting, Vadose Zone J., 18, 1-10,

817   10.2136/vzj2018.08.0148, 2019.

818   Stewart, R. D., Abou Najm, M. R., Rupp, D. E., and Selker, J. S.: Modeling multidomain hydraulic properties of shrink-swell soils,

819   Water Resour. Res., 52, 7911-7930, 10.1002/2016wr019336, 2016b.

820   Stewart, R. D., Rupp, D. E., Abou Najm, M. R., and Selker, J. S.: A Unified Model for Soil Shrinkage, Subsidence, and Cracking,

821   Vadose Zone J., 15, 1-15, 10.2136/vzj2015.11.0146, 2016a.

822   Tian, B.-G., Cheng, Q., Tang, C.-S., Zeng, H., Xu, J.-j., and Shi, B.: Effects of compaction state on desiccation cracking behaviour

823   of a clayey soil subjected to wetting-drying cycles, Eng. Geol., 302, 10.1016/j.enggeo.2022.106650, 2022.

824   Tichavsky, R., Ballesteros-Canovas, J. A., Silhan, K., Tolasz, R., and Stoffel, M.: Dry Spells and Extreme Precipitation are The

825   Main Trigger of Landslides in Central Europe, Sci Rep, 9, 14560, 10.1038/s41598-019-51148-2, 2019.

826   Tuong, T. P., Cabangon, R. J., and Wopereis, M. C. S.: Quantifying Flow Processes during Land Soaking of Cracked Rice Soils,

827   Soil Sci. Soc. Am. J., 60, 872-879, 10.2136/sssaj1996.03615995006000030028x, 1996.

828   van Genuchten, M. T.: A Closed-form Equation for Predicting the Hydraulic Conductivity of Unsaturated Soils, Soil Sci. Soc. Am.

829   J., 44, 892-898, 10.2136/sssaj1980.03615995004400050002x, 1980.

830   van Genuchten, M. T. and Wierenga, P. J.: Mass Transfer Studies in Sorbing Porous Media I. Analytical Solutions, Soil Sci. Soc.

831   Am. J., 40, 473-480, 10.2136/sssaj1976.03615995004000040011x, 1976.

832   Vervoort, R. W., Silburn, M., and Kirby, M.: Near surface water balance in the Northern Murray-Darling Basin, Water Sci. Technol.,

833   48, 207-214, 10.2166/wst.2003.0442, 2003.

834   Vogel, T., Gerke, H. H., Zhang, R., and Van Genuchten, M. T.: Modeling flow and transport in a two-dimensional dual-permeability

835   system with spatially variable hydraulic properties, J. Hydrol., 238, 78-89, 10.1016/s0022-1694(00)00327-9, 2000.

836   Wang, C., Zhang, Z.-y., Fan, S.-m., Mwiya, R., and Xie, M.-x.: Effects of straw incorporation on desiccation cracking patterns and

837   horizontal flow in cracked clay loam, Soil Tillage Res., 182, 130-143, 10.1016/j.still.2018.04.006, 2018.

838   Wang, Z., Liu, J., Hamoud, Y. A., Wang, Y., Qiu, R., Agathokleous, E., Hong, C., and Shaghaleh, H.: Natural (15)N abundance as

839   an indicator of nitrogen utilization efficiency in rice under alternate wetting and drying irrigation in soils with high clay contents,

840   Sci Total Environ, 838, 156528, 10.1016/j.scitotenv.2022.156528, 2022.

841   Weiler, M.: An infiltration model based on flow variability in macropores: development, sensitivity analysis and applications, J.

842   Hydrol., 310, 294-315, 10.1016/j.jhydrol.2005.01.010, 2005.

843   Wen, T., Wang, P., Shao, L., and Guo, X.: Experimental investigations of soil shrinkage characteristics and their effects on the soil

844   water characteristic curve, Eng. Geol., 284, 10.1016/j.enggeo.2021.106035, 2021.

845   Wilson, G. W., Fredlund, D. G., and Barbour, S. L.: The effect of soil suction on evaporative fluxes from soil surfaces, Canadian

846   Geotechnical Journal, 34, 145-155, 10.1139/t96-078, 1997.

847   Xie, C., Ni, P., Xu, M., Mei, G., and Zhao, Y.: Combined measure of geometry optimization and vegetation for expansive soil slopes,

848   Comput. Geotech., 123, 10.1016/j.compgeo.2020.103588, 2020.

849   Xu, J.-J., Tang, C.-S., Cheng, Q., Vahedifard, F., Liu, B., and Shi, B.: Monitoring and early detection of soil desiccation cracking

850   using distributed fibre optical sensing, Géotechnique, 1-12, 10.1680/jgeot.21.00397, 2022.

851   Xu, J.-J., Tang, C.-S., Cheng, Q., Xu, Q.-l., Inyang, H. I., Lin, Z.-Y., and Shi, B.: Investigation on desiccation cracking behavior of

852   clayey soils with a perspective of fracture mechanics: a review, J. Soils Sediments, 22, 859-888, 10.1007/s11368-021-03082-y, 2021.

853   Zhang, J., Luo, Y., Zhou, Z., Victor, C., and Duan, M.: Research on the rainfall-induced regional slope failures along the Yangtze

854   River of Anhui, China, Landslides, 18, 1801-1821, 10.1007/s10346-021-01623-7, 2021a.

855   Zhang, J., Luo, Y., Zhou, Z., Chong, L., Victor, C., and Zhang, Y.: Effects of preferential flow induced by desiccation cracks on

856   slope stability, Eng. Geol., 288, 10.1016/j.enggeo.2021.106164, 2021b.

857